Original Manuscript

SHM Structural Health Monitoring

Brillouin scattering spectrum-based crack measurement using distributed fiber optic sensing

Structural Health Monitoring
2021, Vol. 0(0) 1–22

DOI: 10.1177/14759217211030913
journals.sagepub.com/home/shm
SAGE

Ruonan Ou[1], Linqing Luo[1,2] and Kenichi Soga[1]

Abstract

Brillouin scattering-based distributed fiber optic sensing (Brillouin-DFOS) technology is widely used in health monitoring of large-scale structures with the aim to provide early warning of structural degradation and timely maintenance and renewal. Material cracking is one of the key mechanisms that contribute to structural failure. However, the conventional strain measurement using the Brillouin-DFOS system has a decimeter-order spatial resolution, and therefore it is difficult to measure the highly localized strain generated by a sub-millimeter crack. In this study, a new crack analysis method based on Brillouin scattering spectrum (BSS) data is proposed to overcome this spatial resolution-induced measurement limitation. By taking the derivative of the BSS data and tracking their local minimums, the method can extract the maximum strain within the spatial resolution around the measurement points. By comparing the variation of the maximum strain within the spatial resolution around different measurement points along the fiber, cracks can be located. The performance of the method is demonstrated and verified by locating and quantifying a small gap created between two wood boards when one of the wood boards is pushed away from the other. The test result verifies the accuracy of the crack strain quantification of the method and proves its capability to measure a sub-millimeter crack. The method is also applied to a thin bonded concrete overlay of asphalt pavement field experiment, in which the growth of a transverse joint penetrating through the concrete–asphalt interface was monitored. The method successfully locates the position, traces the strain variation, and estimates the width of a crack less than 0.1 mm wide using a Brillouin-DFOS system with 750 mm spatial resolution.

Keywords

Brillouin scattering spectrum decomposition, distributed fiber optic sensing, crack analysis, concrete pavement, BOTDA/R

Introduction

Detecting the development of cracks in a structure is a crucial part of its structural health monitoring in the context of evaluating safety.[1] Generation of unwanted cracks affects the integrity and service life of the structure.[2–4] It is important to conduct effective monitoring of cracks because the early detection helps reduce the risk of such structural failure.[3] In the past, a variety of monitoring techniques have been proposed and adopted to detect crack development in a structure; they include acoustic emission,[5] infrared thermography,[6] ground penetrating radar,[7] fiber Bragg grating,[8] digital image correlation,[9] and computer vision.[10] As the timing and position of crack opening are usually unforeseen, a solution that has wide coverage and allows continuous monitoring will be attractive.

Distributed fiber optic sensing technology provides distributed strain and temperature measurements over a long distance along the cable.[11] It can be a good candidate for continuous monitoring of cracks with wide coverage. For instance, the Brillouin optic frequency domain analysis was used to monitor the opening and closing of segment joints in a shield tunnel.[12] The Rayleigh scattering-based optical backscatter reflectometer (OBR) was adopted to measure a narrow crack of 0.05 mm inside a reinforced concrete bar under eccentric tension,[1] whereas the pulse pre-pump Brillouin optic time domain analysis (PPP-BOTDA) was

[1]Civil and Environmental Engineering, University of California Berkeley, Berkeley, CA, USA
[2]Earth and Environmental Sciences Area, Lawrence Berkeley National Laboratory, Berkeley, CA, USA

Corresponding author:
Linqing Luo, Earth and Environmental Sciences Area, Lawrence Berkeley National Laboratory, #1 Cyclotron Road, MS 74R316C, Berkeley, CA 94720-8099, USA.
Email: linqingluo@lbl.gov

used to monitor the delamination of ultra-high-performance concrete overlay by installing optical fibers vertically and searching for a sharp peak within the strain reading.[13] In these studies, a crack-induced localized strain was diagnosed by taking advantage of the fine spatial resolution of the analyzers; the spatial resolutions of the OBR and PPP-BOTDA systems are 5 mm and 20 mm, respectively. However, there is a tradeoff between spatial resolution and maximum sensing distance[14] as the maximum sensing distance of a technique with fine spatial resolution (such as OBR and PPP-BOTDA) is usually short. For example, the OBR and PPP-BOTDA systems can only provide a strain profile of a fiber optic cable length of 70 m and 500 m, respectively.[1,13] In a large-scale field application of more than the km range, it is preferred to use a system based on Brillouin optical time domain reflectometer (BOTDR) or Brillouin optic time domain analysis (BOTDA) because it can measure a continuous strain profile along the fiber optic cable of tens of kilometers.[11]

As illustrated in Figure 1(a), the BOTDA/R system provides the Brillouin scattering spectrum (BSS) at each measurement point. The conventional strain analysis utilizing the BOTDA/R system is based on the strain profile converted from the profile of the central frequencies of the BSSs measured at sampling points. These systems have a spatial resolution of between 0.5 m and 1 m. When a crack occurs within a spatial resolution section of a sampling point, the reading is affected by both the background strain and crack strain. As the size of the crack is often much smaller than the spatial resolution, the corresponding BSS is primarily influenced by the dominant background strain instead of the localized crack strain. Hence, at a given sampling point, the strain value derived from the central frequency of the BSS is close to the dominant strain value[15,16] rather than the crack strain value. Therefore, it is difficult to detect cracks by performing the conventional strain profile analysis of BOTDA/R systems.

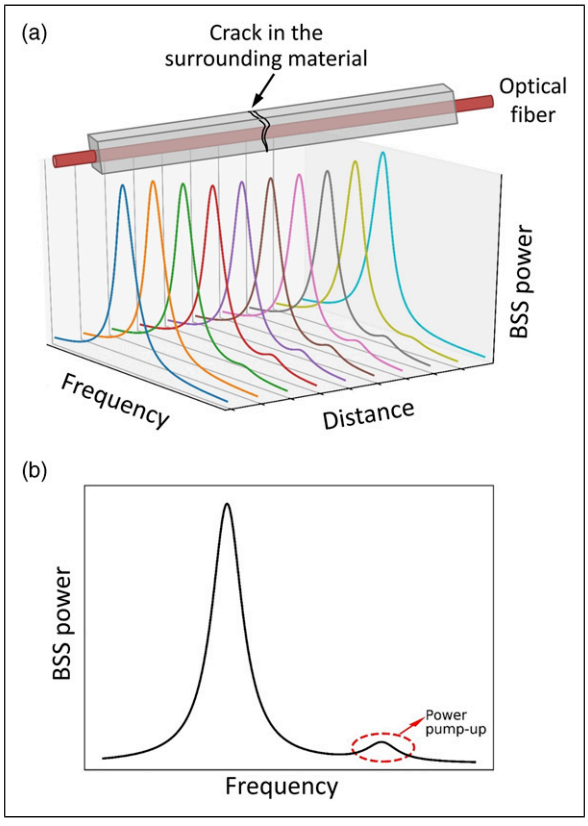

Figure 1. Measurements from BOTDA/R system (a) BSSs along the optical fiber (b) BSS at the position of crack. BOTDA/R: Brillouin optic frequency domain analysis/R; BSS: Brillouin scattering spectrum.

The power distribution at each frequency in the BSS reflects all the strain information within the spatial resolution.[15,17,18] A localized tensile strain induces a small power pump-up at a higher frequency of the BSS, as shown in Figure 1(b). Utilizing this, a multi-peak fitting method has been proposed to extract the tensile strain information of a crack from the BSS by fitting the secondary peak at a higher frequency to a Lorentzian function.[19] However, this method is only valid for a BSS with a clear double-peak feature, and this only appears when the crack strain value is very large, as shown in the figure. At the early stage of crack opening, the strain value at the crack location is small, and the peak of the small power pump-up is too close to the main peak to induce a secondary peak.[15,17] Hence, to give an early warning of crack generation, an alternative data interpretation method is needed.

In the following sections of this article, a new BSS-based method is introduced to perform crack analysis. The section Principle of Brillouin Scattering-Based Fiber Optic Sensing Technology presents the principle of Brillouin-DFOS technology and BSS. In the section BSS-based Crack Analysis Methodology, the theoretical analysis of the BSS measurement from a BOTDA/R system with a large spatial resolution is given. The analysis result links the change in the BSS to crack strain and size and deduces a relationship between BSS at different positions and crack position. It provides the theoretical basis of the new BSS-based crack analysis method. A step-by-step procedure of the method is also given. The section Wood Board Separation Laboratory Test shows the capability of the method in locating a crack and quantifying its size from a laboratory experiment of a synthetic crack opening. To demonstrate the practical engineering application of the method, the section Joint Propagation Analysis of Thin Bonded Concrete Overlay of Asphalt (BCOA) describes a field test of monitoring crack propagation through the concrete–asphalt interface of a thin BCOA pavement.

Principle of Brillouin scattering-based fiber optic sensing technology

When light travels in an optical fiber, a portion of it is always scattered because of the interaction of the electromagnetic field (photon) with impurities or density fluctuation within the fiber, as shown in Figure 2. A portion of the backscattered light exchanges the power with the local mass oscillations (phonon) so that the frequency is slightly shifted, which is called Brillouin scattering.[20–22] Brillouin scattering-based fiber optic sensing technology takes advantage of the Brillouin scattering. The frequency shift of the scattered light is given by[20,22]

$$v_B = \frac{2nv_a}{\lambda} \tag{1}$$

where v_a is the acoustic velocity, n is the refractive index of the fiber, and λ is the wavelength of the incident light.

Since v_a is proportional to the strain and temperature change,[23,24] v_B can be expressed as

$$v_B(\varepsilon,T) = v_B(\varepsilon_r,T_r) + C_\varepsilon(\varepsilon - \varepsilon_r) + C_T(T - T_r) \tag{2}$$

where C_ε is the strain coefficient, C_T is the temperature coefficient, and ε_r and T_r are the reference strain and temperature, respectively. Due to the exponential decay of the acoustic waves, Brillouin gain has a Lorentz-shape profile[15,18,25]

$$g(v,v_B) = g_0\frac{v^2}{(v - v_B)^2 + \Delta v^2} \tag{3}$$

where v is the half-width at half-maximum, g_0 is Brillouin gain coefficient, and v_B is the central frequency.

There are two major types of Brillouin scattering-based DFOS systems: BOTDR and BOTDA. Both inject a pulse light into one end of the optical fiber and measure the power gain and loss of the Brillouin scattering signal in the time domain. The spatial resolution L is determined by the nonzero input pulse width[22]

$$L = \frac{c\tau}{2n} \tag{4}$$

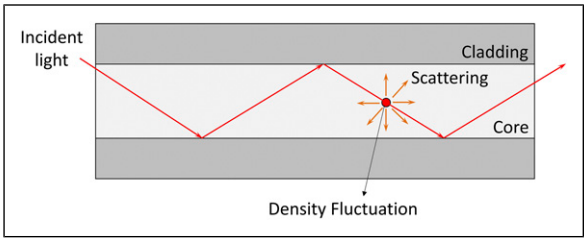

Figure 2. Principle of light scattering in the single-mode fiber.

where c is the light velocity in the vacuum, τ is the pulse width, and n is the refractive index of the fiber core.

The middle point of the pulse corresponds to the measurement (i.e., sampling) point.[26,27] The strains of the fiber covered by the optical pulse are convoluted within the spatial resolution, and as a result, the BSS is integrated under the optical pulse. The interrogator measured BSS can be assumed to be an average of the uniform distribution of local Brillouin gain within the spatial resolution.[15,18,28] By ignoring the attenuation and pump depletion,[29] the BSS at the measurement point can be simplified as the integration of the local Brillouin gain over the spatial resolution around it[15,18,28]

$$G(v,Z) = \frac{1}{L}\int_{Z-\frac{L}{2}}^{Z+\frac{L}{2}} g(v,v_B(z))dz \tag{5}$$

where Z is the measurement point position. In the rest of the article, spatial resolution window (SRW) is defined as the area within L around each measurement point. The distance between the two adjacent measurement points is the readout interval, which is determined by the time interval between two consecutive sampling points digitized by the instrument.[11]

As shown in equation (4), the spatial resolution can be improved by narrowing the pulse width. However, the pulse width that is shorter than the lifetime of the acoustic photon will not gain or lose the full energy of the acoustic phonon, leading to the abrupt drop in the accuracy of strain readings.[11,22] Therefore, the minimum spatial resolution of the BOTDR and BOTDA systems is usually limited to be between 0.5 m and 1.0 m. To make the measurement results accurate, a sophisticated fitting process is commonly conducted to the measured BSS.[30] At a given measurement point, the BSS is fitted to a mathematical expression and the central frequency is calculated by locating the maximum power point. The derived central frequency is translated into the strain and temperature measurement by equation (2). The BOTDA/R system provides both BSSs and the strain and temperature profile along the sensing section of the fiber optic cable.

BSS-based crack analysis methodology

Problem formulation

Figure 3 shows a crack that is generated in the middle of a $3L$ long sensing section of optical fiber, which is three times the spatial resolution, L. At the crack opening location, the fiber is under the peak strain and fully debonded with the surrounding material. In the vicinity of the crack, slippage happens between the fiber and the structure when the crack is large. The fiber is partially debonded from the material near the opening area forming a transition zone between the

crack and the dominant strain (l_c in the figure).[1] In this study, for simplicity, the strain profile is assumed to take a triangle shape with peak strain, ε_c, in the middle to simulate crack generation. The spatial ratio of the slippage area comparing with the spatial resolution is $r_c = l_c/L$. The rest of the fiber (non-cracking) is under the uniform strain, ε_d. The integration of the distributed strains within the crack area is the size of the crack opening d_c

$$d_c = 0.5(\varepsilon_c - \varepsilon_d) r_c L \tag{6}$$

From equation (6), to quantify the size of the crack (d_c), ε_c and r_c need to be extracted. Therefore, to accomplish the crack analysis, the following three parameters need to be derived from the raw BSS measurement data: (1) the peak strain of the crack, ε_c; (2) the spatial ratio of the slippage area around the crack, r_c; and (3) the position of the crack. The following subsections theoretically derive the crack analysis method that aims to quantify these parameters from the BSS measurements provided by the BOTDA/R system.

Evaluating ε_c from BSS

Crack-induced BSS deformation. When a strain profile shown in Figure 3 is given, $G(v)$ at location Z, in which the SRW fully covers the triangle in the strain profile becomes the black solid curve in Figure 4(a). By substituting equation (3) into equation (5), $G(v)$ is given by

$$G(v) = \frac{1}{L}\int_{Z-\frac{L}{2}}^{Z+\frac{L}{2}} g_0 \frac{\Delta v^2}{\left(v - v_B(\varepsilon(z))\right)^2 + \Delta v^2} dz \tag{7}$$

It is the superposition of the weighted spectrum of every strain value happening within it (the dashed curves). The weights of the spectrums of ε_d (dominant strain: blue dotted line), ε_c (peak strain: red dash-dot line), and ε_{tr} (strains in the transition zone: black dashed lines) are r_{ε_d}, r_{ε_c}, and $r_{\varepsilon_{tr}}$ in the figure, respectively. The weights are reflected by the proportion of the given strain within the SRW. In Figure 4(a), the right bound of the concave area coincides with the inflection point of the BSS.

From equation (7), the first derivative of BSS is given by

$$G'(v) = \frac{dG(v)}{dv} = \frac{1}{L}\int_{Z-\frac{L}{2}}^{Z+\frac{L}{2}} g_0 \frac{-2\Delta v^2 \cdot \left(v - v_B(\varepsilon(z))\right)}{\left(\left(v - v_B(\varepsilon(z))\right)^2 + \Delta v^2\right)^2} dz \tag{8}$$

The first derivatives of the BSS (black solid line) and of the spectrums of ε_c and ε_d (red dash-dot line and blue dotted line, respectively) are plotted in Figure 4(b). The spectrum gradient of ε_c and ε_d intersect with the x-axis at $v_B(\varepsilon_c)$ and $v_B(\varepsilon_d)$, respectively. The BSS gradient shows two local minimums; the one on the left corresponds to the concave area around the maximum point, whereas the other on the right is induced by the crack generation. In the rest of the article, the frequency coordinate of the latter local minimum of the BSS gradient is defined as v_{Bm}. v_{Bm} can be converted to the corresponding strain ε_{cm} according to equation (2). It is noted that, under a different set of normalized crack width $r_c = l_c/L$ and crack peak strain ε_c, v_{Bm} may not be exactly equal to $v_B(\varepsilon_c)$. The relationship between the two is discussed in the following two subsections so that the geometrically derived ε_{cm} from the BSS data can be converted to the true crack peak strain ε_c.

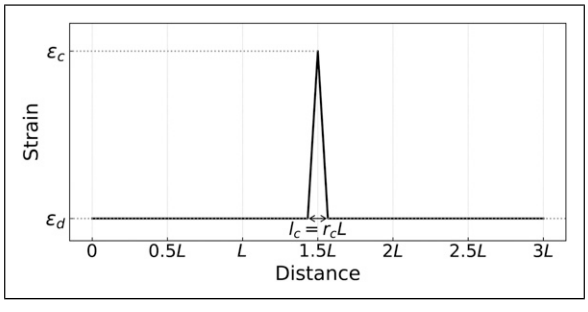

Figure 3. Simulated strain profile of crack.

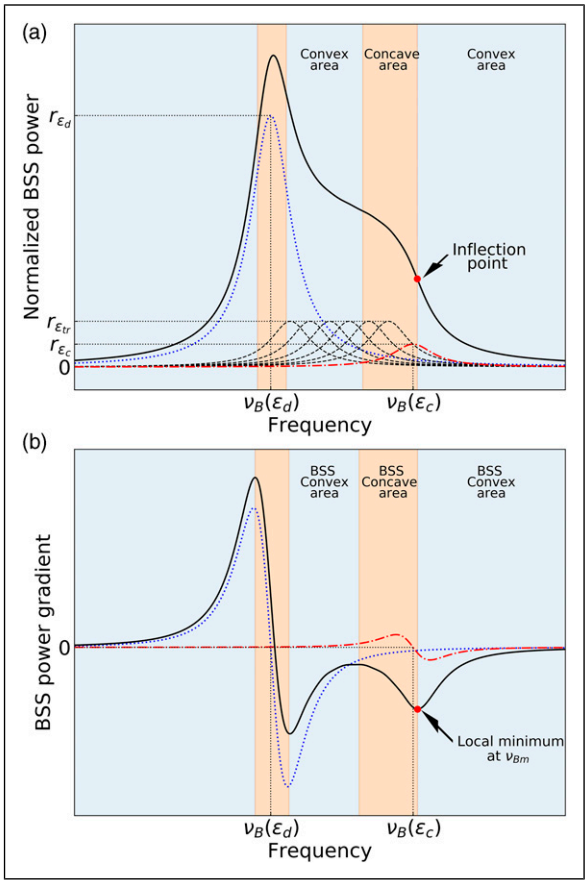

Figure 4. (a) BSS of the SRW that fully covers the crack and (b) the corresponding BSS gradient. BSS: Brillouin scattering spectrum; SRW: spatial resolution window.

Crack detection limit. The number of concave areas in $G(\nu)$, which is also the number of the local minimums in $G'(\nu)$, depends on two factors. The first factor is the difference between ε_c and ε_d. As shown in Figure 4(a), the two concave areas of $G(\nu)$ are around $\nu_B(\varepsilon_d)$ and $\nu_B(\varepsilon_c)$, respectively. When $\varepsilon_c - \varepsilon_d$ is small, the two concave areas overlap each other and form a single concave area. In this case, only one local minimum can be found in $G'(\nu)$. The second factor that affects the number of local minimums in $G'(\nu)$ is the spatial ratio r_c of the stressed area induced by the crack.

Figure 5 shows $G(\nu)$ and the corresponding $G'(\nu)$ under different r_c values when $\varepsilon_c - \varepsilon_d = 3000\,\mu\varepsilon$ ($\nu_B(\varepsilon_d) = 10.8$ GHz, $\nu_B(\varepsilon_c) = 10.95$ GHz) for a typical analyzer parameter ($\Delta\nu = 0.05$ GHz and $C_\varepsilon = 499.8$ MHz/%). As shown in Figure 5(a), when r_c is small (blue solid line: $r_c = 0.1$, giving small slippage), $G(\nu)$ has only one concave area near $\nu_B(\varepsilon_d)$. The superposition of the spectrums within the stressed area induced by the crack (triangle area in the strain profile in Figure 3) is not large enough to induce another concave area near $\nu_B(\varepsilon_c)$. Hence, as shown in Figure 5(b), there is only one local minimum in $G'(\nu)$ along the blue line with its position near $\nu_B(\varepsilon_d)$.

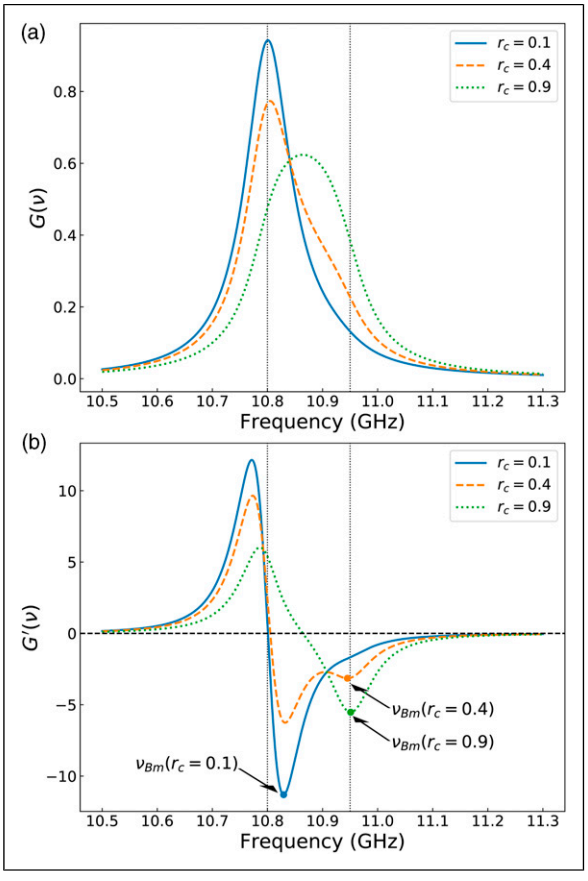

Figure 5. (a) BSS and (b) BSS gradient under different r_c when $\nu_B(\varepsilon_d) = 10.8$ GHz, $\nu_B(\varepsilon_c) = 10.95$ GHz, $\nu = 0.05$ GHz, and $C_\varepsilon = 499.8$ MHz/%. BSS: Brillouin scattering spectrum.

When r_c is large (green dotted line: $r_c = 0.9$, giving large slippage), the BSS power is affected more on the frequencies corresponding to the tensile strains generated by the crack. Under this condition, only one concave area exists along $G(\nu)$ in Figure 5(a), and the frequency coordinate of its corresponding local minimum along $G'(\nu)$ in Figure 5(b), ν_{Bm}, is close to $\nu_B(\varepsilon_c)$. Only when r_c is of intermediate value (orange dashed line: $r_c = 0.4$), two concave areas appear along $G(\nu)$ in Figure 5(a). ν_{Bm} is the frequency coordinate of the local minimum on the right of $G'(\nu)$ in Figure 5(b) and ν_{Bm} is close to $\nu_B(\varepsilon_c)$.

By giving $\Delta\nu = 0.05$ GHz and $C_\varepsilon = 499.8$ MHz/% (a typical setting of BOTDA analyzer), the critical combinations of $\varepsilon_d - \varepsilon_c$ and r_c at which $G'(\nu)$ switches from the single to the double local minimum are the black curve plotted in Figure 6. Over the curve, double local minimums are present. For example, when $r_c = 0.3$, the second minimum appears at $\varepsilon_c - \varepsilon_d > 2790\,\mu\varepsilon$. Below the curve, only one local minimum is observed and it is divided into two zones by $r_c = 0.428$ (dashed line). When $r_c < 0.428$, the single minimum ν_{Bm} is near $\nu_B(\varepsilon_d)$; this is the case of $r_c = 0.1$ in Figure 5. Under this condition, ν_{Bm} is affected largely by $\nu_B(\varepsilon_d)$ and hence cannot be used to estimate ε_c. When $r_c > 0.428$, ν_{Bm} is close to $\nu_B(\varepsilon_c)$; this is the case of $r_c = 0.9$ in Figure 5. Therefore, only when $\varepsilon_d - \varepsilon_c$ and r_c are within the orange dotted and green back slashed areas in Figure 6, ν_{Bm} can be related to $\nu_B(\varepsilon_c)$ and a crack can be detected.

In engineering applications, crack size is the primary concern. Since the crack width d_c depends on $(\varepsilon_c - \varepsilon_d)$ (see equation (6)), the strain graph shown in Figure 6 can be converted to the normalized crack size graph (d_c/L) as shown in Figure 7. The orange dotted, green back slashed, and blue slashed areas in Figure 7 correspond to the areas in the same color and hatch in Figure 6, respectively. It is possible to estimate the detectable crack size using this figure. For example, assuming $L = 1$ m, for $r_c = 0.3$, the secondary minimum appears when d_c is larger than $0.42 \times 10^{-3} L = 0.42$ mm, which is the minimum detectable crack size.

Correction from ε_{cm} to ε_c. As mentioned at the end of the section Problem Formulation, $(\nu_{Bm} = \nu_B(\varepsilon_{cm}))$ evaluated from the local minimum of the spectrum data may not be exactly equal to $\nu_B(\varepsilon_c)$. A correction from ε_{cm} to ε_c is therefore needed. Through a series of simulations of BSS and the BSS gradient in which the strain profile within $(L,2L)$ in Figure 3 under different r_c and $\varepsilon_c - \varepsilon_d$ values are used for equation (8), ν_{Bm} (and hence ε_{cm}) under different r_c and $\varepsilon_c - \varepsilon_d$ are evaluated. The simulation results are used to develop a theoretically driven relationship between $(\varepsilon_{cm} - \varepsilon_d)$ (measured from the local minimum data analysis)

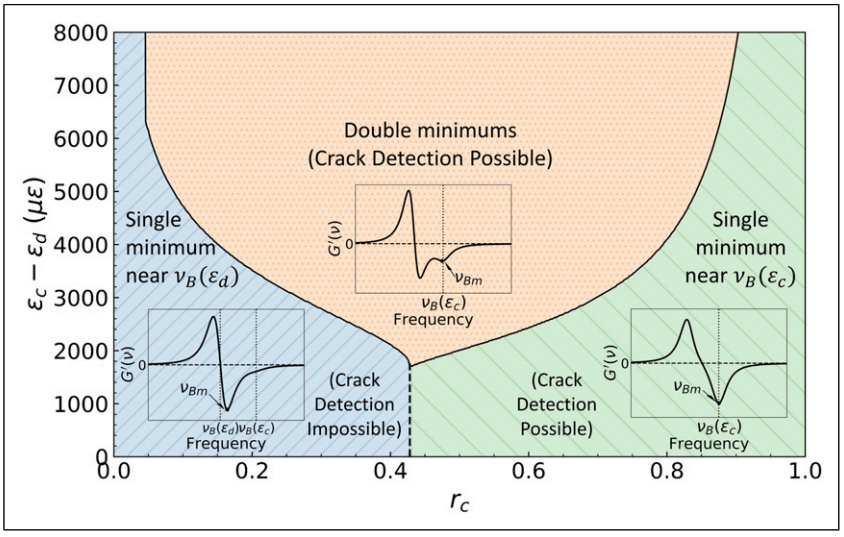

Figure 6. Single to double-minimum transition curve of $\varepsilon_c - \varepsilon_d$ and r_c.

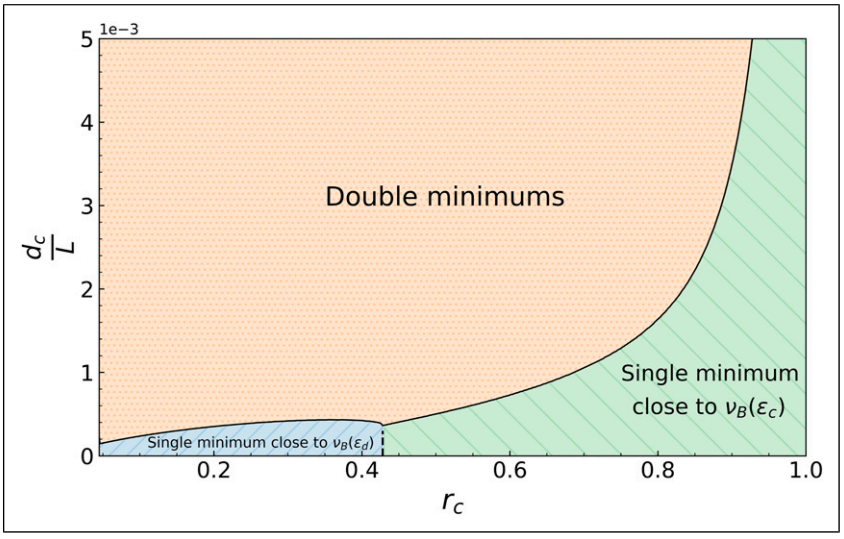

Figure 7. Single to double-minimum transition curve of r_c and d_c/L.

and $(\varepsilon_c - \varepsilon_d)$ (true crack strain), as shown in Figure 8 (when $r_c < 0.428$) and Figure 9 (when $r_c \geq 0.428$) for the condition of a typical analyzer setting ($\Delta\nu = 0.05\,\text{GHz}$ and $C_\varepsilon = 499.8\,\text{MHz}/\%$).

If r_c is known, $(\varepsilon_{cm} - \varepsilon_d)$ can be converted to $(\varepsilon_c - \varepsilon_d)$ using Figure 8 or 9. For the case of $r_c < 0.428$ in Figure 8, $(\varepsilon_c - \varepsilon_d)$ can be determined for a given r_c when $(\varepsilon_{cm} - \varepsilon_d)$ is above the grey dashed line, which corresponds to the double-minimum range (orange dotted area in Figures 6 and 7). For the case of $r_c \geq 0.428$ in Figure 9, all the points are within either the orange dotted area or the green back slashed area in Figures 6 and 7 where ν_{Bm} is close to $\nu_B(\varepsilon_c)$. As $(\varepsilon_{cm} - \varepsilon_d)$ increases (or crack size increases), it becomes asymptotic to the actual value of $(\varepsilon_c - \varepsilon_d)$.

All the curves in Figures 8 and 9 intersect with the y-axis at 577.58 $\mu\varepsilon$. When $\varepsilon_c - \varepsilon_d = 0$, the strain value is equal to ε_d at all the positions within the SRW. By substituting the flat strain profile with the strain values equating to ε_d into equation (7), $G'(\nu) = g_0 - 2\Delta\nu^2 \cdot (\nu - \nu_B(\varepsilon_d))/((\nu - \nu_B(\varepsilon_d)^2) + \Delta\nu^2)^2$. In this case, $G'(\nu)$ is with only one local minimum and ν_{Bm} corresponds to the larger solution of $G''(\nu) = 0$. $G''(\nu) = g_0 2\Delta\nu^2 \cdot (3(\nu - \nu_B(\varepsilon_d))^4 + 2\Delta\nu^2(\nu - \nu_B(\varepsilon_d))^2 - \Delta\nu^4)/((\nu - \nu_B(\varepsilon_d))^2 + \Delta\nu^2)^2 = 0$ has two solutions, $\nu_B(\varepsilon_d) - \sqrt{3}\Delta\nu/3$ and $\nu_B(\varepsilon_d) + \sqrt{3}\Delta\nu/3$. This is the

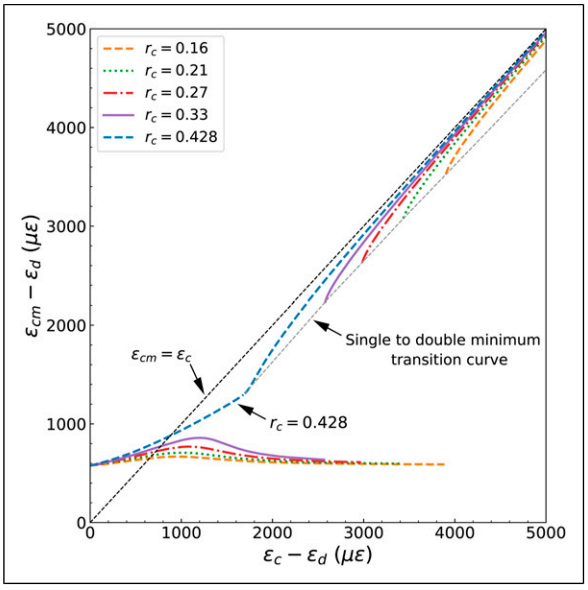

Figure 8. Correction chart from $\varepsilon_{cm} - \varepsilon_d$ to $\varepsilon_c - \varepsilon_d$ for $r_c < 0.428$ when $v = 0.05$ GHz and $C_\varepsilon = 499.8$ MHz/%.

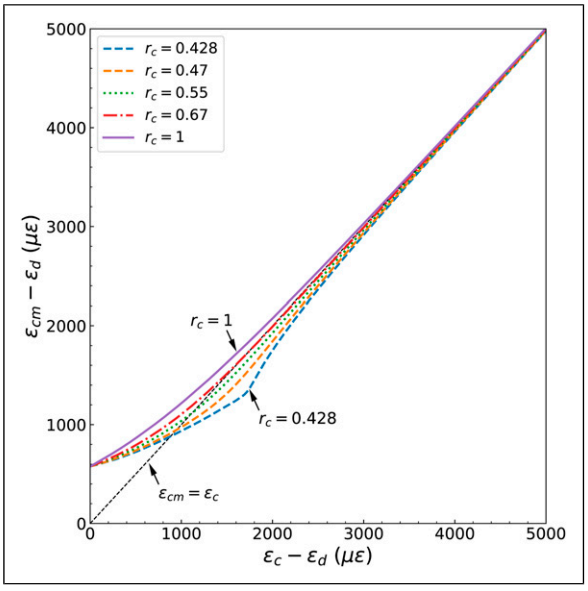

Figure 9. Correction chart from $\varepsilon_{cm} - \varepsilon_d$ to $\varepsilon_c - \varepsilon_d$ for $r_c \geq 0.428$ when $v = 0.05$ GHz and $C_\varepsilon = 499.8$ MHz/%.

local minimum under the uniform strain condition. The strain equivalent of $\frac{\sqrt{3}}{3}\Delta v$ is $\sqrt{3}\Delta v/3C_\varepsilon = \sqrt{3}(0.05\,\text{GHz})/3(499.8\,\text{MHz}/\%) = 577.58\ \mu\varepsilon$.

Locating crack position and evaluating $\boldsymbol{r_c}$

To find the location of the crack, it is proposed to check the profile of ε_m, which is defined as maximum strain within the SRW of a given measurement point, along the fiber. For example, the profile of ε_m for the strain profile in Figure 3 at different measurement points is plotted in Figure 10. The subplots in the figure mark the coverage of the SRWs at measurement points A to E. Because the SRWs of the measurement points within $(L,2L)$ cover the peak strain of crack, ε_m from L to $2L$ is equal to ε_c in the figure (e.g., point C). The width of $\varepsilon_m = \varepsilon_c$ is equal to the spatial resolution, and the peak strain of the crack happens at the center of this section. When the SRW does not include the peak strain but covers part of the transition zone (e.g., points B and D), the maximum strain within it will be smaller than ε_c but larger than ε_d. For the SRWs that only cover the non-cracking area (e.g., points A and E), ε_m is equal to ε_d. If the ε_m profile is given, the locations of the crack opening zone, the partially debonding zone, and non-cracking zone can be evaluated. The central position of the crack opening zone is then the crack location, which is point C in the case shown in Figure 10. As the total width of the crack opening zone and the partially debonding zone in the ε_m profile is $L + r_cL$ (between $L - r_cL/2$ and $2L + r_cL/2$), r_c can be determined by evaluating this length from the ε_m profile.

As the ε_m profile from the actual crack strain profile given in Figure 3 is not known before analysis, it is proposed to estimate the ε_m profile from the ε_{cm} profile as shown in Figure 11. The proof of the equivalency is given in Appendix 1. In Figure 11, the ε_{cm} profile (red solid line) is obtained by calculating the BSS gradients of all the SRWs and locating the local minimums of them as described in the previous section. The figure also shows the actual ε_m profile as black solid line. Within the non-cracking zone, ε_{cm} is equal to $\varepsilon_d + \sqrt{3}\Delta v/3C_\varepsilon$ as described in the section Locating Crack Position and Evaluating $\boldsymbol{r_c}$. Between L and $2L$, the ε_{cm} profile is flat and linked to ε_c as illustrated in Figures 8 and 9.

The ε_{cm} profile at measurement points of which the SRW covers the partially debonding zone is affected by the crack detection limit described in the section Evaluating 3.2 From BSS. In the lower part of the transition zone below the crack detection limit in Figure 11, the SRW of the measurement points in this part only covers the lower small strain portion of the partially debonding zone and hence it is within the blue slashed area of Figure 6. Crack detection is therefore not possible and the ε_{cm} value in this part is evaluated to be ε_d. In the upper part of the transition zone, however, the ε_{cm} value is detectable from the BSS data. The intersections between the extensions of the slope zones of the ε_{cm} profile (red dashed lines) and $\varepsilon = \varepsilon_d$ are very close to the inflection points (black points) of the ε_m profile. The total width of the extended slopes can then be used to quantify r_cL by extending the slope zones on both sides of the ε_{cm} profile till $\varepsilon = \varepsilon_d$.

The red solid line in Figure 11 shows the ε_{cm} profile when the readout interval of the BOTDA/R system is small; that is, the ε_{cm} profile is constructed by a large number of measurement points. However, when the readout interval is

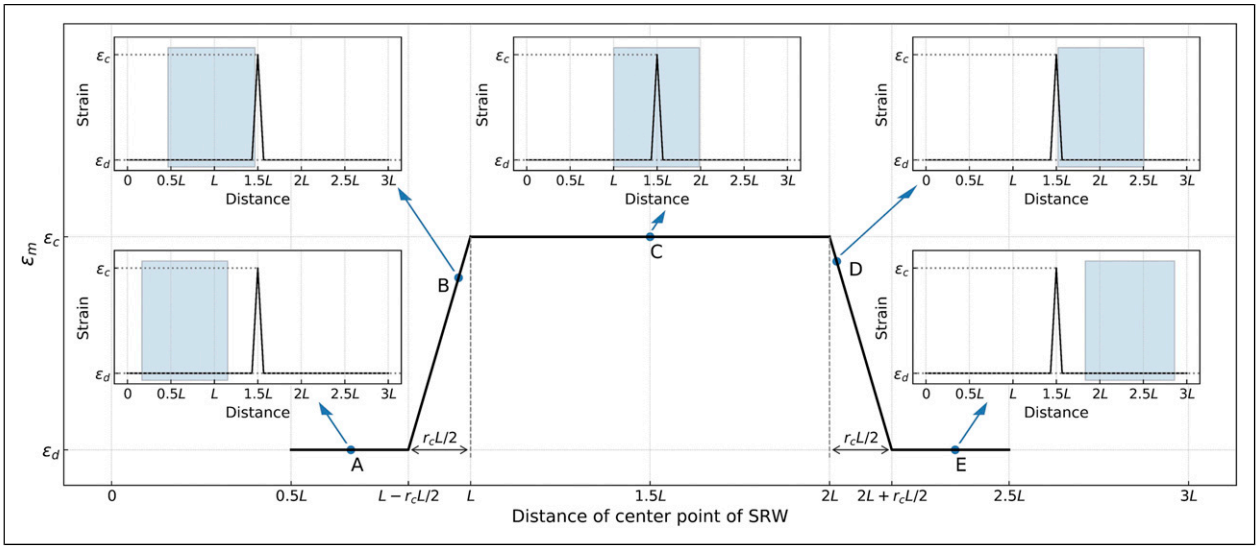

Figure 10. ε_m profile of spatial resolution windows along the fiber.

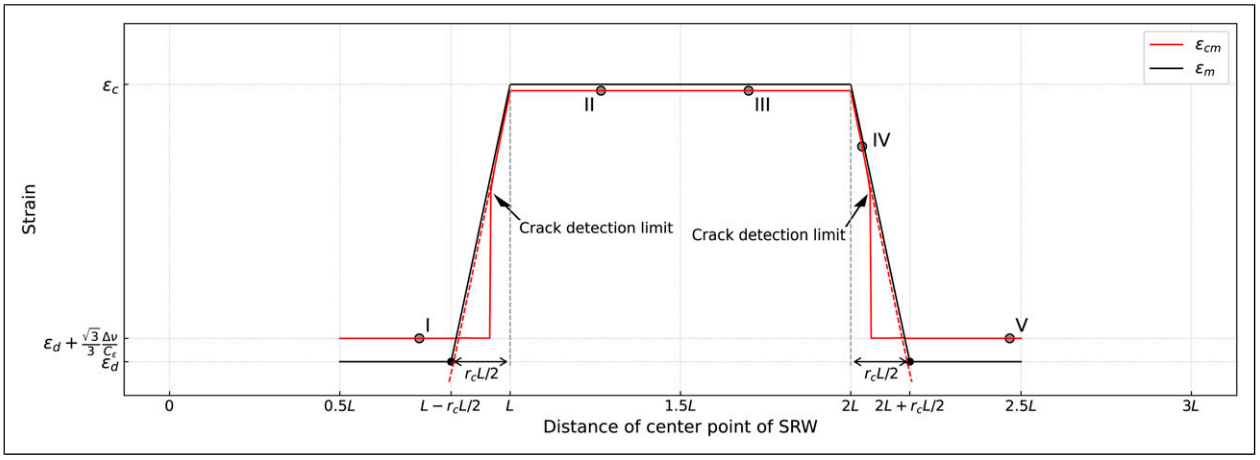

Figure 11. ε_{cm} profile and ε_m profile of spatial resolution windows along the fiber.

large, as shown by the grey points I to V in Figure 11, the ε_{cm} profile only consists of discrete points since the density of the measurement points is not high enough. Among these discrete points, points I and V provide the information of the minimum ε_{cm} of the non-cracking area; points II and III represent the maximum ε_{cm} of the SRWs covering ε_c. Although point IV is within the slope zone of the ε_{cm} profile, the exact shape of the slope zone is still unknown. In this case, the boundary of the flat crest of the ε_{cm} profile needs to be located first to quantify r_c. Since the length of this flat section is equal to the spatial resolution L, the range of it can be located from the position of points II and III. By drawing a line connecting the located right boundary of the flat section and point IV and extend it till $\varepsilon = \varepsilon_d$, r_c can be quantified. When point IV is also missing and only points I, II, III, and V are left, the ε_{cm} profile only contains its maximum value and minimum value. In this case, the range of r_c can only be quantified from Figure 6 using the information of the number of local minimums of the BSSs and the value of the maximum ε_{cm}. The procedure of quantifying r_c from the discrete ε_{cm} profile is carefully demonstrated in the case study given in the section Wood Board Separation Laboratory Test.

In summary, the proposed crack analysis is done from the BSS data using the steps shown in Figure 12.

Wood board separation laboratory test

Experiment setup and test procedure

The ability to locate and quantify a crack using the BSS-based crack analysis method introduced in the section BSS-

based Crack Analysis Methodology is demonstrated by conducting a wood board separation laboratory test in this section. The section BSS-based Crack Analysis Methodology describes the method through the theoretical derivation of the relationship between the BSS data and crack strain and size. It also describes the step-by-step analysis procedure in Figure 12 for practical implementation. This section demonstrates the validity of the method by following the steps given in Figure 12 on a synthetic crack generation made in the laboratory. The capability and limitation of the method are shown by comparing the result with the data provided by a fine spatial resolution interrogator system.

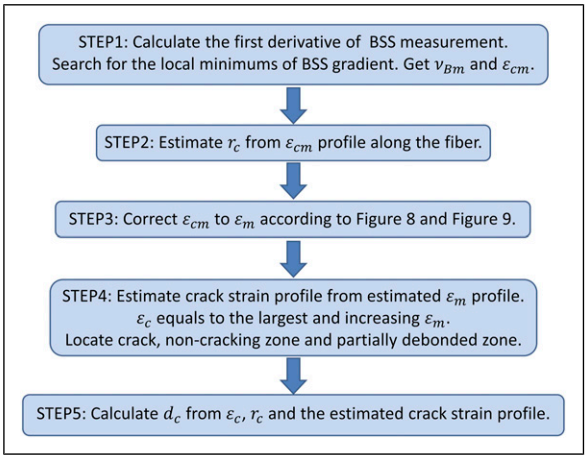

Figure 12. Brillouin scattering spectrum-based crack analysis steps.

As shown in Figures 13(a) and 13(b), two 1 m-long wood boards were put side by side tightly in the longitudinal direction and fixed on a calibration rig. The fixation stand for the left wood board was immobile, while the one for the right board was removable by the screw at the right end of the calibration rig. The gap between the two boards was adjusted to be zero initially. Crack generation was simulated by expanding the gap. The displacement of the right board was controlled by the screw with a precision of 0.01 mm.

Two fiber optic cables were epoxy-glued along the wood boards longitudinally right after setting the initial zero-gap. The two cables were attached parallel to each other with a distance of 1 mm. Both of them were 0.9 mm-diameter single-mode tight buffer strain cable manufactured by Nanzee Ltd. The cross section is shown in Figure 14. The central frequency of the cable with no strain applied is 10.857 Hz, whereas $C_\varepsilon = 499.8\,\mathrm{MHz}/1\%$ and $C_T = 0.915\,\mathrm{MHz}/°\mathrm{C}$.

The two cables were connected to two different commercial interrogators, Omnisens DITEST (Figure 15(a)) and LUNA Technologies ODiSI6104 (Figure 15(b)), to take measurements during the test. Their specifications are listed in Table 1. The LUNA system took strain measurements at every 1.3 mm along the cable. Taking advantage of the 1.3 mm gauge length, its measurements were treated as the ground truth value and used as the reference when evaluating the crack analysis result. The Omnisens system provided BSS at every 250 mm with the spatial resolution

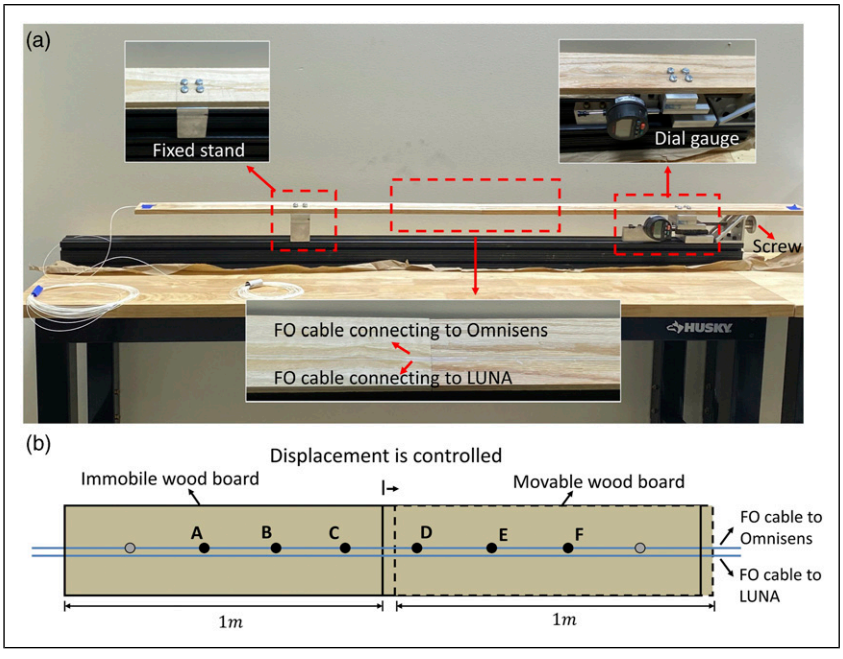

Figure 13. Wood boards setup and fiber optic cables layout (a) photo and (b) schematic.

of 750 mm under the BOTDA mode and v is 0.05 GHz. Since the two cables were installed parallel to each other with a small horizontal distance in between, it was assumed that the two cables measured the same deformation. The proposed crack analysis method was applied to the BSS measurement data to locate and quantify the crack opening. Then, the crack position and the estimated strain and crack size at each step were compared with the ground truth value measured by the LUNA system.

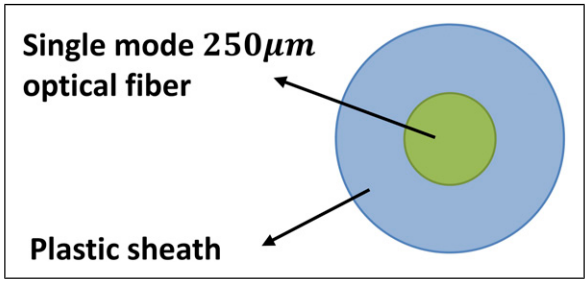

Figure 14. Cross-section of 0.9 mm-diameter single-mode fiber optic cable.

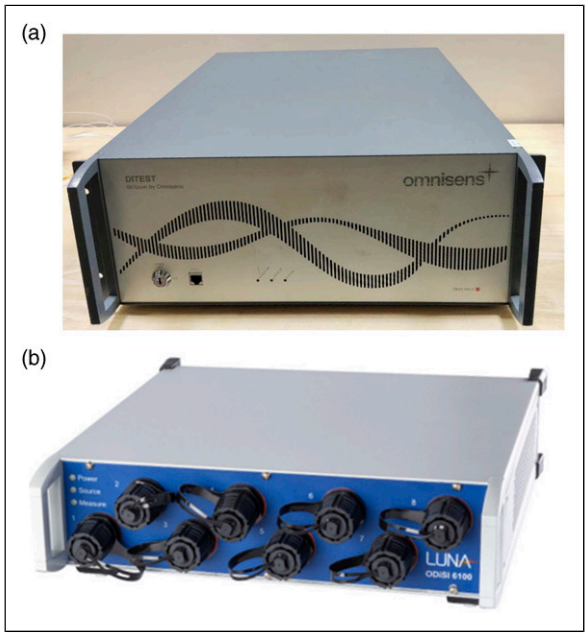

Figure 15. (a) DITEST manufactured by Omnisens (b) ODiSI6104 manufactured by LUNA Technologies.

Results and discussion

Fine spatial resolution interrogator measurement. As shown in Figure 13(b), the Omnisens system provided BSS measurements at six measurement points (points A to F) on the wood boards. In contrast, the LUNA system gave much denser readings (every 1.3 mm), which could be seen as continuous because of its fine spatial resolution and readout resolution. During the test, the right wood board was moved at eleven steps from 0.23 mm to 0.91 mm. The strain measurements taken by the LUNA system under different crack displacements are shown in Figure 16. The largest strain at the crack location, ε_c, rises to up to 10564 $\mu\varepsilon$. The length of the slippage area increases from 150 mm to 225 mm; that is, r_c increases from 0.2 to 0.3 as $L = 750$ mm.

In Figure 16, apart from the fine-resolution strain profiles measured by the LUNA system, the SRWs of points A to F by the Omnisens system are also marked by the blocks in different colors. For example, the measurement point A by the Omnisens system is at 0.382 m. SRW-A in the figure covers the area, [0.007 m, 0.757 m], within the spatial resolution (750 mm) around point A. SRW-A and SRW-F only cover the non-cracking area with relatively uniform and constant strain values applied. The largest strain occurs within the overlapping area of the SRWs of points B, C, and D. Within the SRW of point E, when the crack displacement is 0.23 mm, only a small portion of the transition zone of the strain profile is included. As the crack displacement increases, the right bound of the transition zone expands from 1.05 m to 1.125 m and the SRW of point E starts to overlap with the transition zone. The ε_m of SRW-E rises to up to 8819 $\mu\varepsilon$.

Low spatial resolution BOTDA system measurement. The BSSs at points A to F from the Omnisens system are plotted in Figure 17. At points B, C, D, and E, the peak BSS power decreases, and the power pump-up expands to a higher frequency at the tail part as the crack displacement increases. The spectrums of points A and F do not change with displacement, indicating they are not within the spatial

Table 1. Specifications of Omnisens system and LUNA system.

Parameter	Omnisens DITEST	LUNA Technologies ODiSI6104
Technology	Brillouin scattering-based sensing	Rayleigh scattering-based sensing
Readout resolution	250 mm	1.3 mm
Spatial resolution	750 mm	1.3 mm
Distance range	60 km	50 m

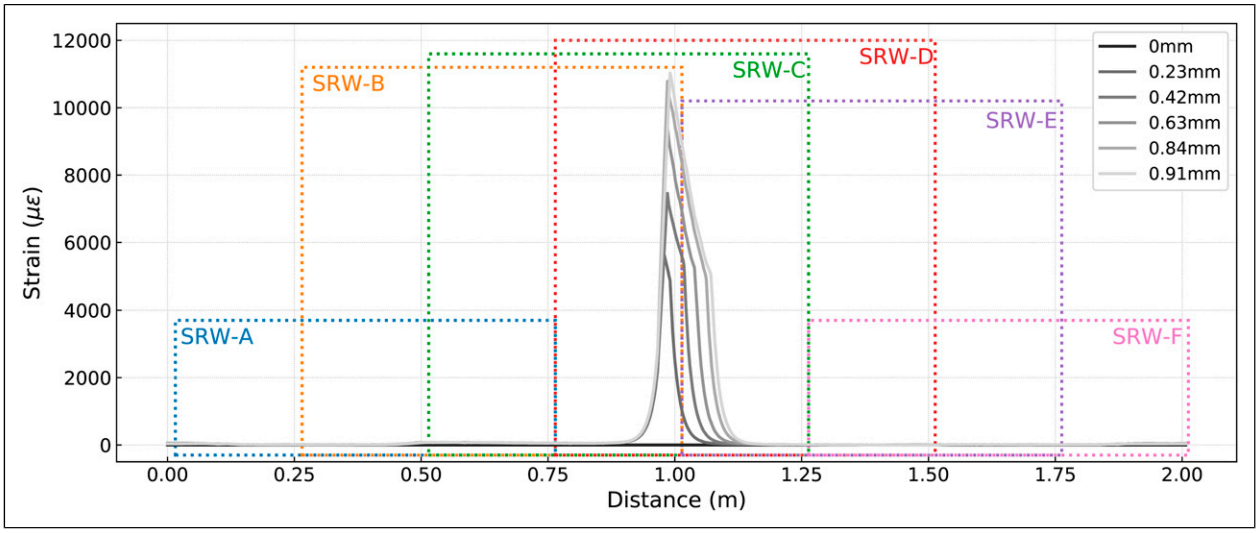

Figure 16. The strain profiles measured by the LUNA system.

resolution around the crack. This is confirmed by the observation within the SRW-A and SRW-F in Figure 16.

Using the BSSs of these measurement points, the proposed crack analysis is performed by following the steps shown in Figure 12.

Step 1 Take the derivatives of the BSS measurements and locate the local minimums to derive ν_{Bm} and ε_{cm}

The values of $\varepsilon_{cm} - \varepsilon_d$ are evaluated using the proposed method at the six measurement points by tracking the frequency coordinates of the local minimums of the gradient of the BSS measurements. To eliminate the fluctuation induced by the noise in the measured spectrums, moving average with a window of 0.005 GHz is applied to the raw data before taking the derivative. The concave areas in the BSSs of points B, C, D, and E are evident as shown in Figure 18. The local minimums induced by the crack are highlighted by the larger marker size.

From the frequency coordinates of the marked local minimums in Figure 18, the values of $\varepsilon_{cm} - \varepsilon_d$ at different crack displacements for the six points are evaluated and plotted in Figure 19. The $\varepsilon_{cm} - \varepsilon_d$ values of SRW-B to SRW-E increase, whereas those of SRW-A and SRW-F keep constant as the crack size expands. This indicates that SRW-B to SRW-E are always within the crack influence region, while SRW-A and SRW-F are out of the crack influence region at all displacement steps. The $\varepsilon_{cm} - \varepsilon_d$ values of SRW-A and SRW-F (the non-cracking area) are around $\sqrt{3}\Delta\nu/3C_\varepsilon = 577.58\ \mu\varepsilon$ as derived in the section Correction From ε_{cm} to ε_c.

Step 2. Estimate r_c from the ε_{cm} profile

In Figure 20, the $\varepsilon_{cm} - \varepsilon_d$ values evaluated in Step 1 are plotted versus the position of the center points of their corresponding SRWs (measurement points A to F) as discrete points which are marked by the larger marker size. Because the readout resolution of the Omnisens system is 250 mm, these discrete data points are not dense enough to form a comprehensive ε_{cm} profile.

When the crack displacement is larger than 0.42 mm, the $\varepsilon_{cm} - \varepsilon_d$ value of SRW-E is between the minimum and the maximum value and hence is on the right slope of the $\varepsilon_{cm} - \varepsilon_d$ profile. As discussed in the section Locating Crack Position and Evaluating $\boldsymbol{r_c}$, the $\varepsilon_{cm} - \varepsilon_d$ profile is constructed using the following constraints (i) the length of the flat crest is 750 mm, which is the spatial resolution length, (ii) intersects the $\varepsilon_{cm} - \varepsilon_d$ values derived in Step 1, and (iii) it is symmetric. Having three points at the flat crest and one point along the transition zone gives a unique profile at a given displacement as shown in the figure. The r_c for the crack displacements larger than 0.42 mm is estimated to be around 0.23. The ground truth data given in Figure 16 show that the right bound of the transition zone keeps at 0.9 m and the left bound moves from 1.07 m to 1.125 m. Hence, the actual r_c for these crack displacements varies from 0.23 to 0.3, indicating the estimation is accurate.

When the crack displacement is 0.23 mm, the discrete ε_{cm} profile only contains its maximum and minimum values. The double minimum feature is observed in the BSS gradient of points B, C, and D, and their $\varepsilon_{cm} - \varepsilon_d$ values are 5272 $\mu\varepsilon$. According to Figure 6, to have a double minimum at this strain level, r_c needs to be larger than 0.076. Since r_c is 0.23 when the crack displacement is larger than 0.42 mm, r_c at this crack displacement is smaller than 0.23. Since there is no additional information to narrow down this range (0.076, 0.23), r_c is estimated to be the middle of this range, 0.153. From Figure 16, the actual r_c at this crack displacement step is 0.2, which is within the estimated range.

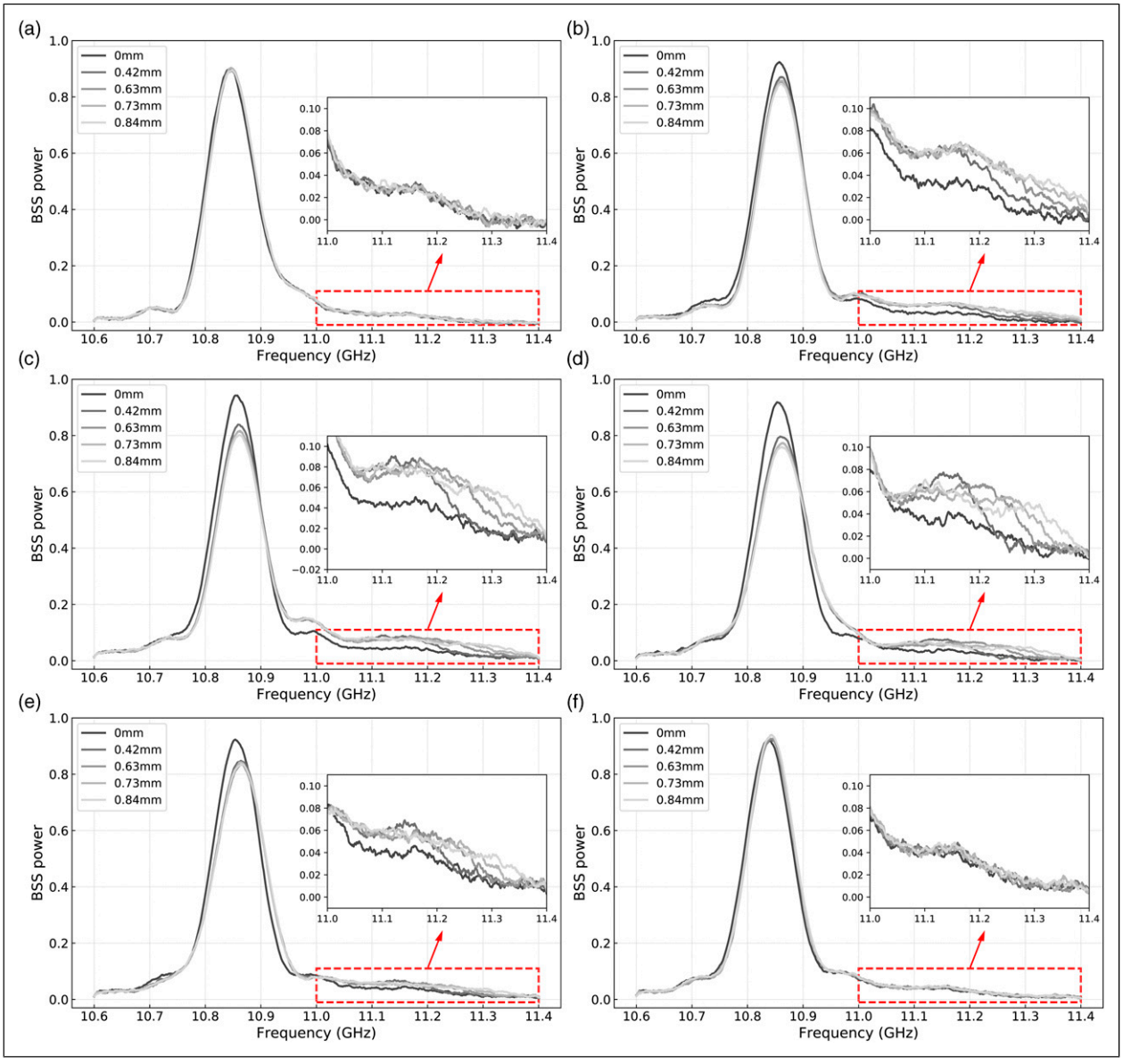

Figure 17. Brillouin scattering spectrums at points A to F at different displacement steps.

Step 3. Correct ε_{cm} to ε_m using Figures 8 and 9

Since v of the Omnisens system and C_ε of the fiber used in this test are the same as those used in the simulation in the section Evaluating $\boldsymbol{\varepsilon_c}$ From BSS, the correction of ε_{cm} to ε_m given in Figures 8 and 9 can be used. As shown in Figure 19, the values of $\varepsilon_{cm} - \varepsilon_d$ of the crack detected measurement points are over 5000 $\mu\varepsilon$. According to Figures 8 and 9, for the estimated r_c from the previous step, $\varepsilon_{cm} - \varepsilon_d$ is very close to the actual value when it is over 5000 $\mu\varepsilon$. Figure 21(a) shows the estimated ε_m of different crack displacements at the six points. The ε_m values at points B, C, and D are the largest and the same, indicating the crack location is within the overlapping area of their corresponding SRWs and ε_c is equal to these values. The ε_m value at point E jumps to 5766 $\mu\varepsilon$ when the crack displacement is 0.42 mm because the r_c value increased, and the SRW of point E overlaps to the partially debonding zone. These behaviors agree with the evaluation made from the LUNA measurements in Figure 16.

Figure 21(b) compares the values of ε_m at points A, C, and E measured by the LUNA system and the estimations made in Figure 21(a). The estimation results match the measured values very well, except for the data at point E when the crack displacement is 0.23 mm. At this displacement, the actual $\varepsilon_m - \varepsilon_d$ of SRW-E is 910 $\mu\varepsilon$ and the actual r_c is 0.074 from the LUNA measurement. This

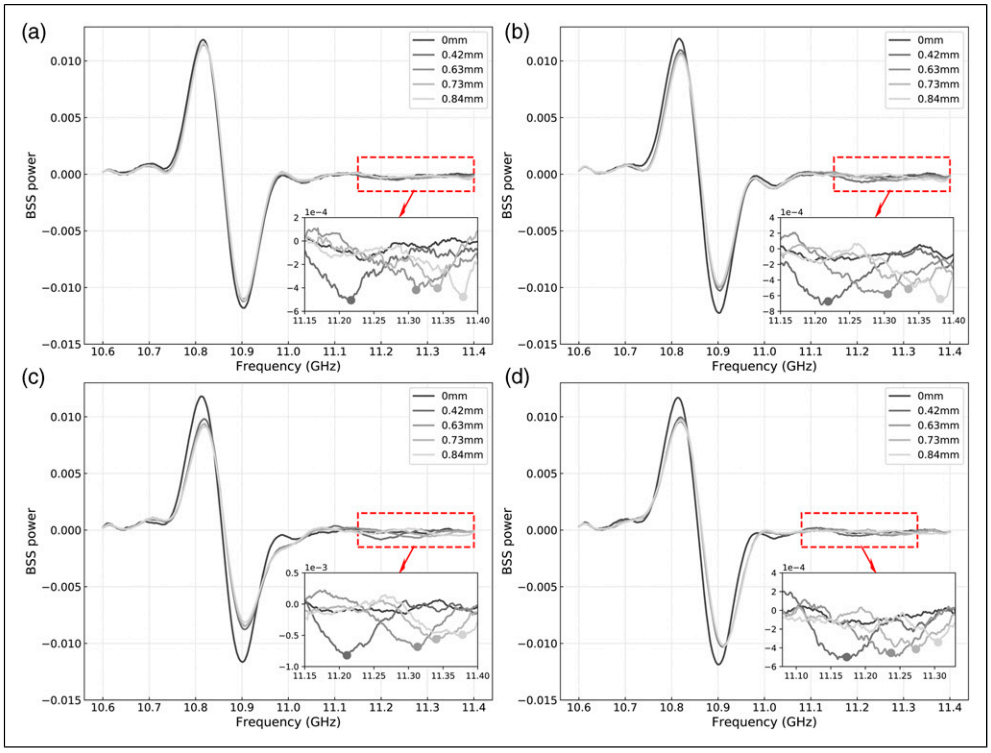

Figure 18. Brillouin scattering spectrum gradients at points B to E at different displacement steps.

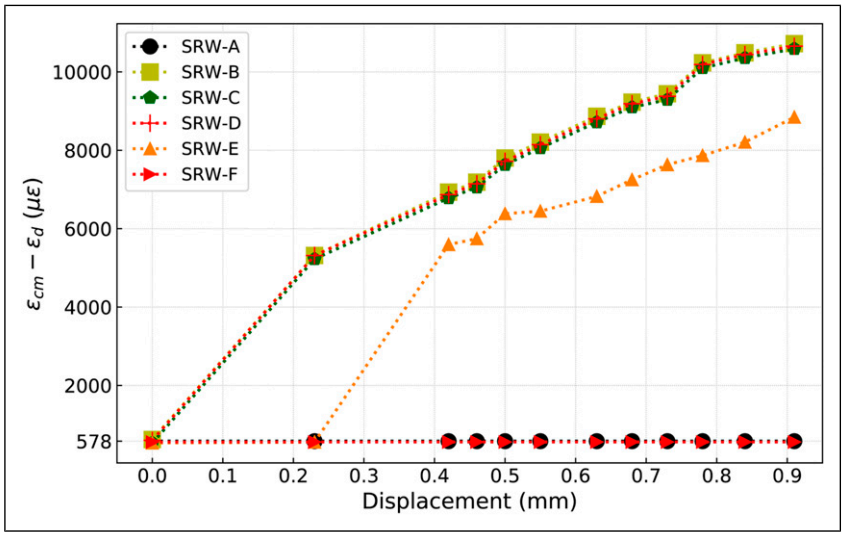

Figure 19. $\varepsilon_{cm} - \varepsilon_d$ of SRW-A to SRW-F at different displacement steps. SRW: spatial resolution window.

combination is in the blue slashed area of Figure 6 where the proposed method cannot detect the crack.

Steps 4. and 5 Estimate the crack strain profile and calculate d_c

From the estimated ε_m and r_c values, the estimated ε_m profile along the fiber is shown in Figure 22(a). ε_c is equal to the maximum value of ε_m within the flat section in the middle of the plot. The crack opening location is evaluated to be at 1m, which is the location where the crack was developed. The strain profile along the fiber is back calculated and plotted in Figure 22(b). Comparing with the strain profile measured by LUNA in Figure 16, the estimated ε_c value matches the actual values well. The strain

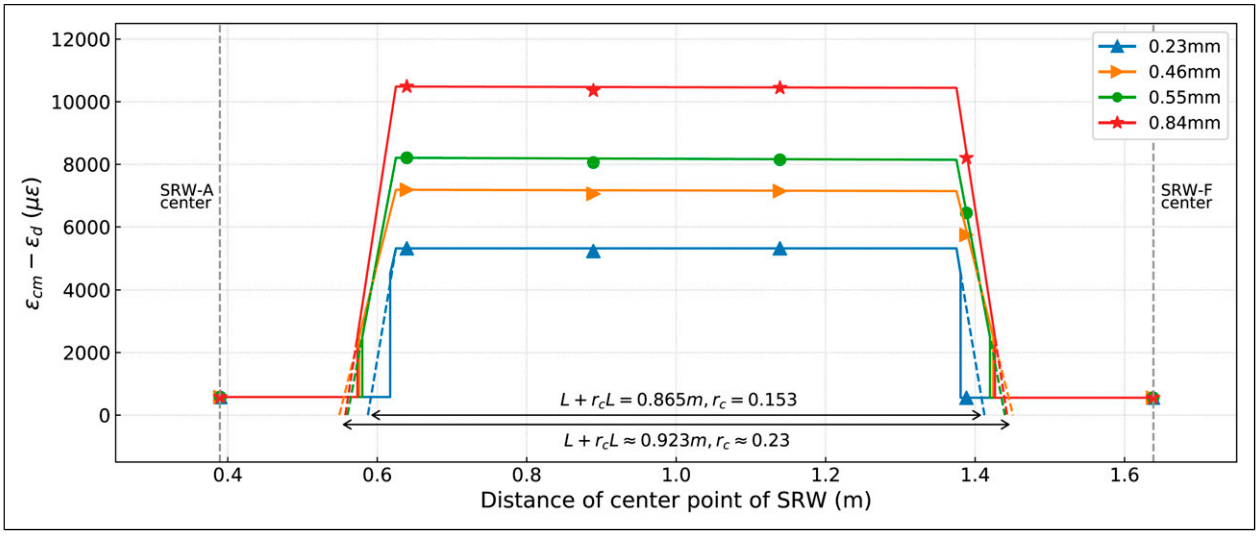

Figure 20. $\varepsilon_{cm} - \varepsilon_d$ profile.

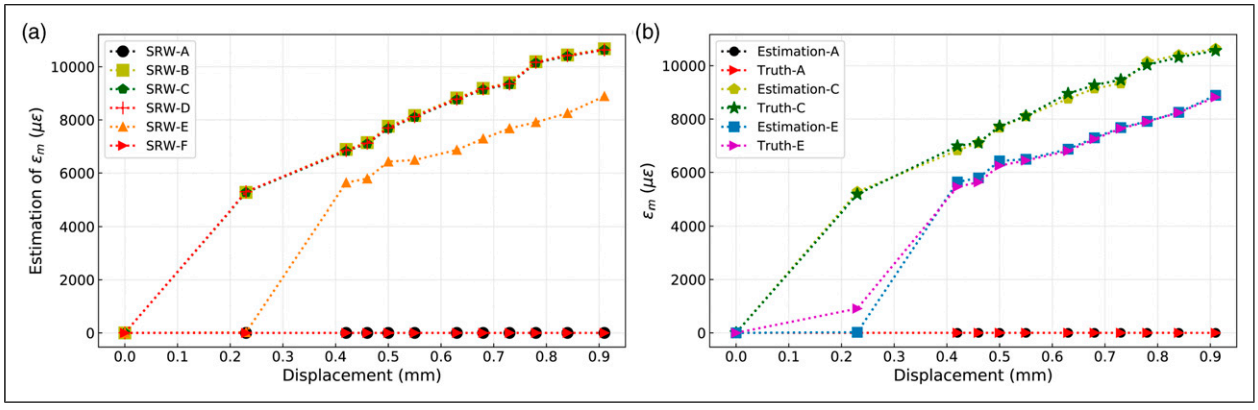

Figure 21. (a) Estimation of ε_m of SRW-A to SRW-F and (b) estimation versus truth value of ε_m of SRW-A, SRW-C, and SRW-E at different displacement steps. SRW: spatial resolution window.

profile between the crack peak strain and the left boundary of SRW-E is a straight line in Figure 22(b). It also matches the truth.

From the strain profile given in Figure 22(b), the crack displacements can be estimated. In Figure 23, the estimated values are compared with (i) the actual crack displacement values from the dial gauge and (ii) the value that is calculated by taking the integral of the LUNA strain profile given in Figure 16. The blue, red, and grey areas in the figure correspond to the 10%, 20%, and 30% estimation error, respectively. The measured crack widths by the LUNA system (black points) match very well with the actual gap widths (blue line), which confirms the feasibility of treating the measurement from the LUNA system as the ground truth. The crack sizes estimated from the BSSs are all within or on the boundary of the 30% estimation error and eight out of eleven of them are with an estimation error of less than 20%, indicating that the proposed method performs well in evaluating the crack size.

Joint propagation analysis of thin bonded concrete overlay of asphalt

Background

In this section, the new method, which was proposed and verified in the sections BSS-based Crack Analysis Methodology and Wood Board Separation Laboratory Test, is applied in a field test to monitor the joint propagation through a thin BCOA pavement.

Thin BCOA is a pavement rehabilitation method that overlays a thin concrete layer on the old asphalt,[31] as shown in Figure 24. In order to avoid any large differential movement between the concrete overlay and the asphalt and

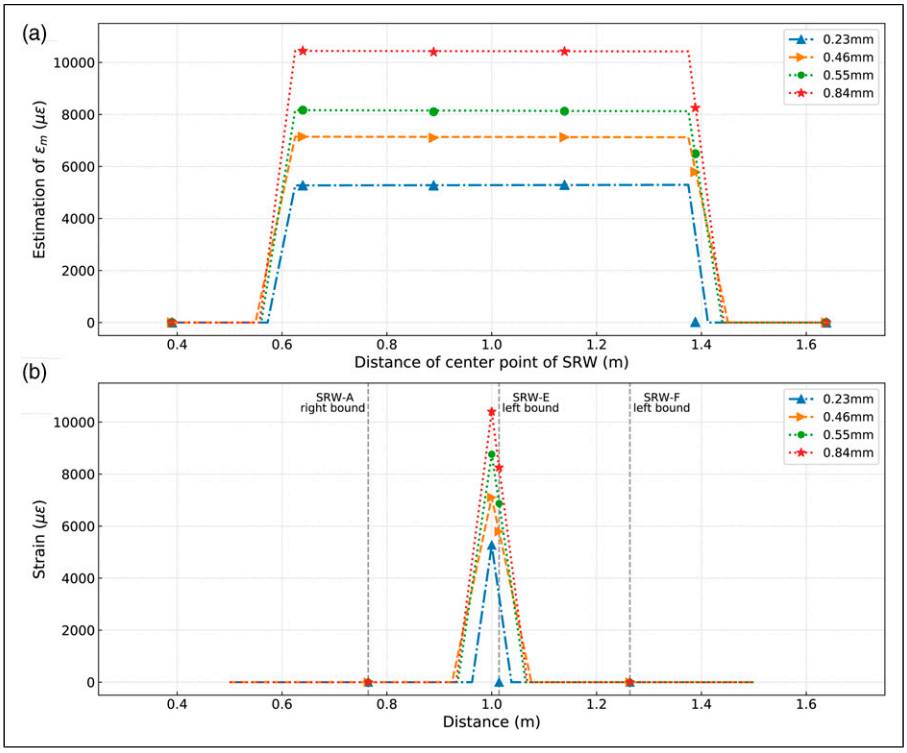

Figure 22. Estimated (a) ε_m profile and (b) strain profile from the proposed method.

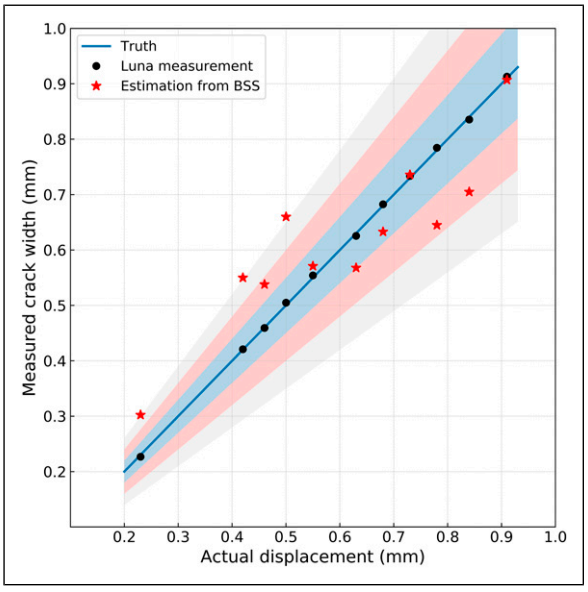

Figure 23. Comparison among the actual gap widths, the measured crack widths from the LUNA system, and the estimated crack widths from the Brillouin scattering spectrums using the proposed method.

curling and warping stresses, joints are sawed on the surface of the concrete layer during construction to divide it into small square slabs, typically with the dimension in the range of 0.9 m to 2.4 m. As shown in the figure, the initial depths of the joints are about one-third of the concrete layer thickness.[32] During its performance life, the joints propagate deeper and may reach the asphalt layer under the long-term traffic loading and the environmental effects.[31] The depth of the joint propagation determines the layer where the faulting, which is one of the main distress mechanisms of BCOA, happens.[31,33] The joint that propagates through the concrete layer leads to the faulting on the asphalt–concrete interface, whereas the joint that propagates through the asphalt layer induces the faulting below the asphalt layer.[33] This part of the study aims to apply the proposed BSS-based crack analysis method to conduct the monitoring and quantification of the joint propagation of BCOA through the concrete layer to the asphalt layer.

Description of the BCOA under test and the sensors layout

The BCOA being tested was constructed at the University of California Pavement Research Center in Davis, CA. It was made of concrete with a dimension of 7.2 m × 1.8 m × 140 mm over a 100 mm thick existing asphalt pavement. As shown in Figure 25, three transverse joints were initially sawed to 40 mm deep to divide the BCOA into four square slabs. Under the large daily temperature variation in autumn, the slabs expanded in the daytime and shrunk at night. The joints propagated deeper as time went by.

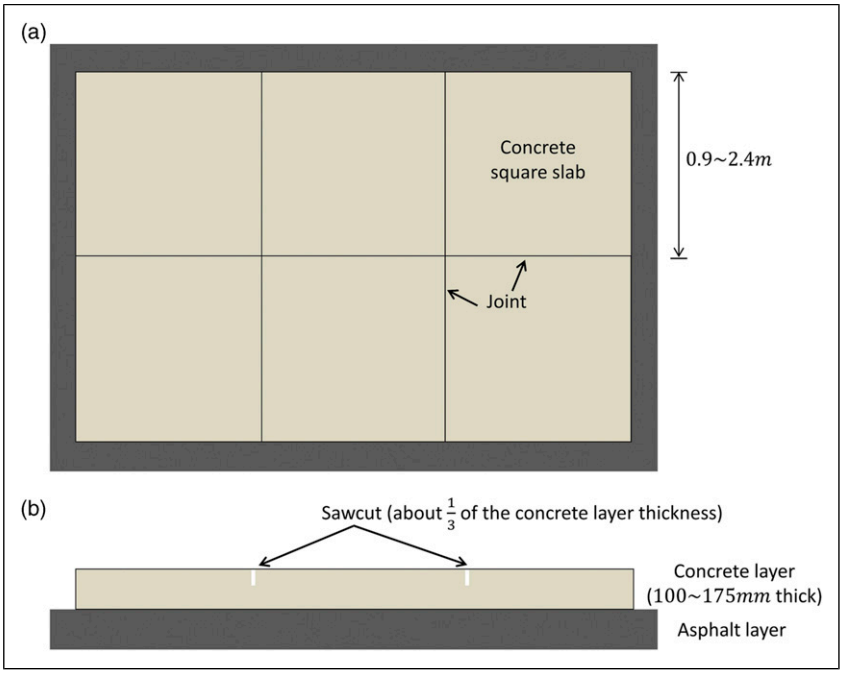

Figure 24. Schematic drawing of thin bonded concrete overlay of asphalt (a) Plan view (b) Main view.

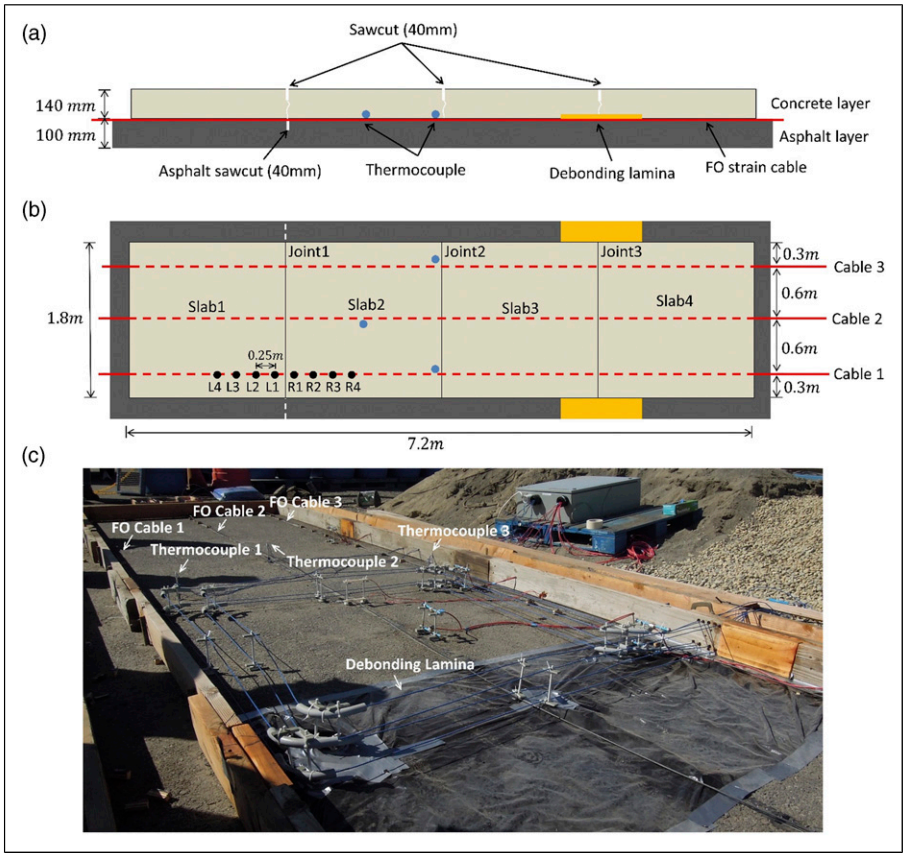

Figure 25. Illustration figure of bonded concrete overlay of asphalt and sensors layout (a) Main view (b) Plan view (c) Site photo.

The three joints were made differently to simulate three different circumstances during the performance life of the BCOA.

1. Joint 1: a transverse sawcut was made on the surface of the asphalt layer at the concrete surface joint location before pouring concrete. It was designed to simulate the joint propagation through the concrete layer to the asphalt layer after long-term traffic loading.
2. Joint 2: it was designed to simulate the short-term condition in which the joint did not penetrate into the asphalt.
3. Joint 3: within 1 m around the joint, a plastic lamina was attached to the existing asphalt to create the debonding between the concrete and the asphalt, which would happen under long-term environmental changes in the field. In this case, the developing joint could not cross the interface.

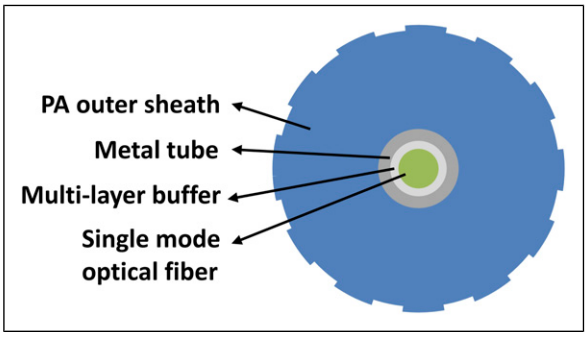

Figure 26. Cross section of 3.2 mm-diameter FO cable.

Only at Joint 1, a crack was expected to cross the concrete–asphalt interface by the daily thermal expansion and contraction of the concrete layer. To monitor and quantify the crack crossing the concrete–asphalt interface, fiber optic strain cables were installed in three longitudinal grooves on the surface of the asphalt layer, as shown in Figure 25. Two of them (Cables 1 and 3) were placed 0.3 m from the two sides, whereas the other one (Cable 2) was placed in the centerline of the BCOA. An armored 3.2 mm-diameter tight-buffered strain cable (Brugg V9) was used to avoid breakage during construction. The cross section of the cable is shown in Figure 26, and the Brillouin parameters are $C_\varepsilon = 450\,\text{MHz}/\%$ and $C_T = 1.1\,\text{MHz}/^\circ\text{C}$.

To record the temperature variation at the interface, three thermal couples were installed next to each fiber separately

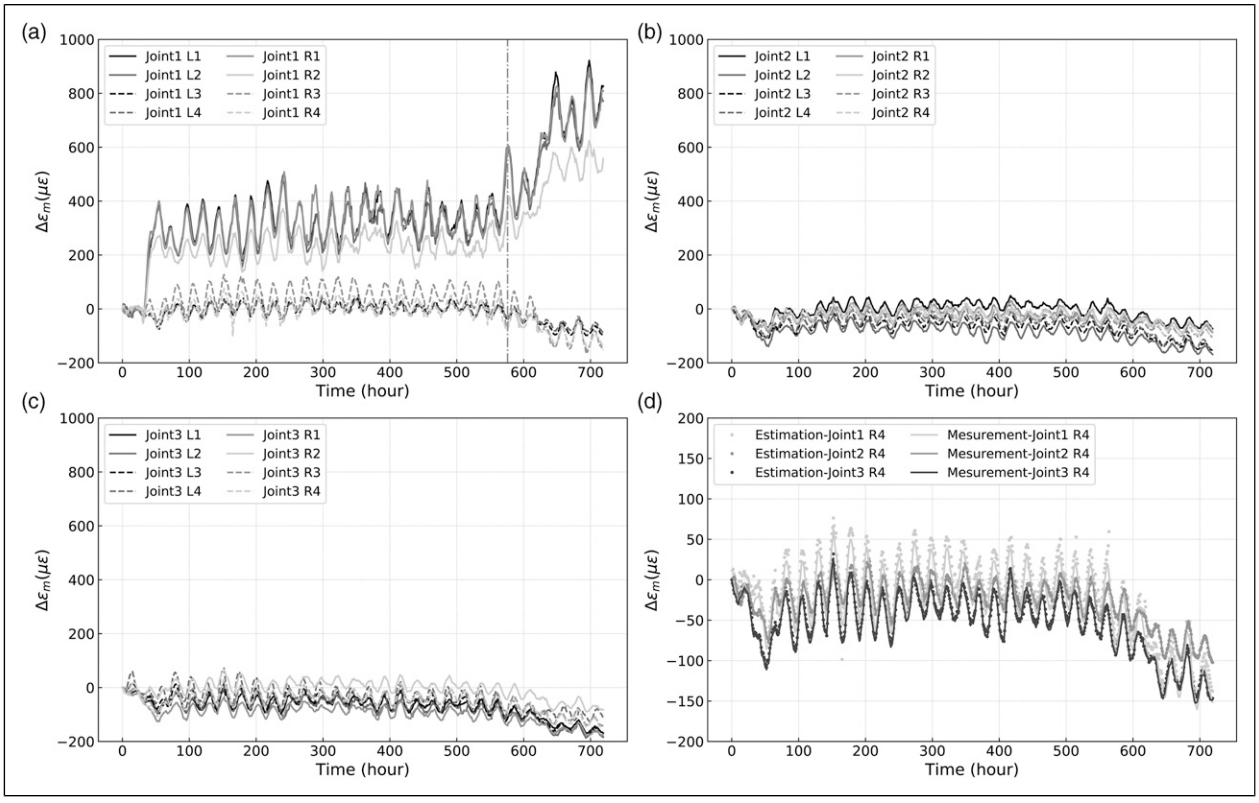

Figure 27. Estimation of ε_m within the eight nearest spatial resolution windows around (a) Joint 1, (b) Joint 2, (c) Joint 3, and (d) estimation values versus measurements of ε_m at R4 of Joint 1, Joint 2, and Joint 3 along Cable 1.

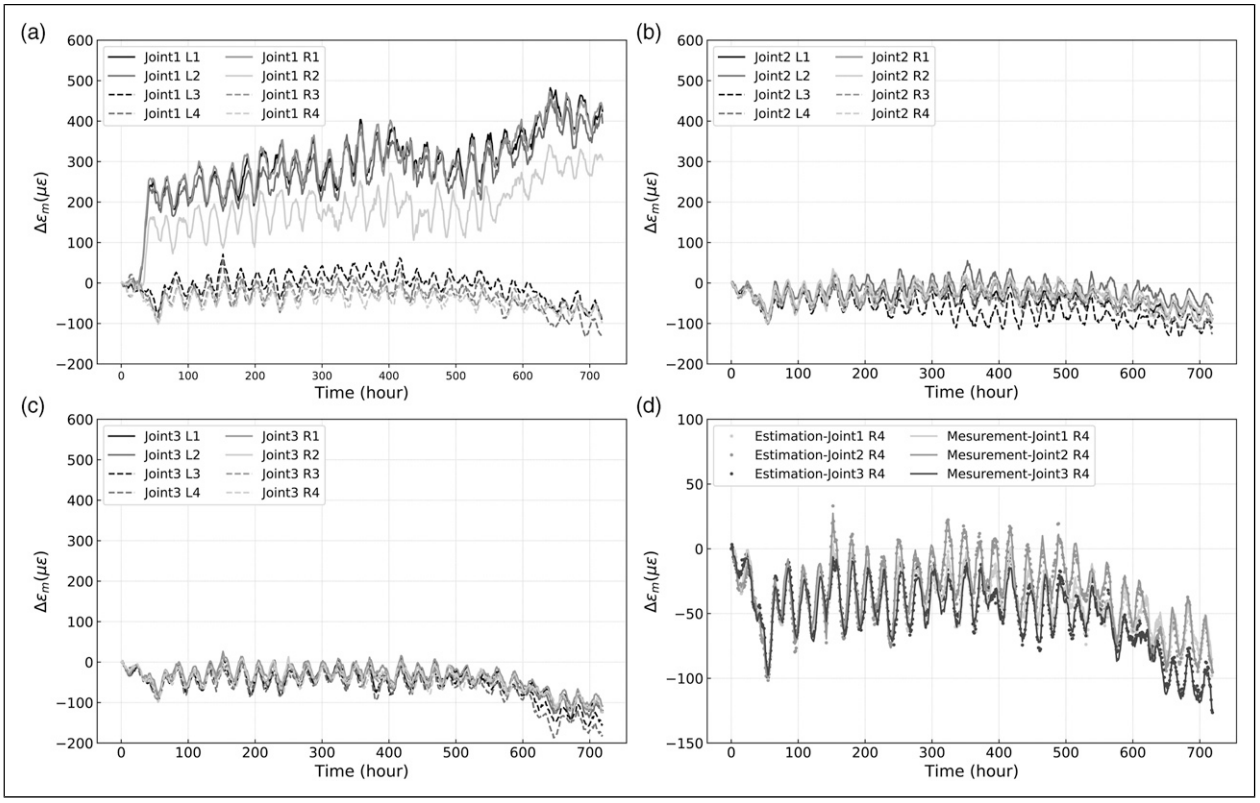

Figure 28. Estimation of ε_m within the eight nearest spatial resolution windows around (a) Joint 1, (b) Joint 2, (c) Joint 3 and (d) estimation values versus measurements of ε_m at R4 of Joint 1, Joint 2 and Joint 3 along Cable 2.

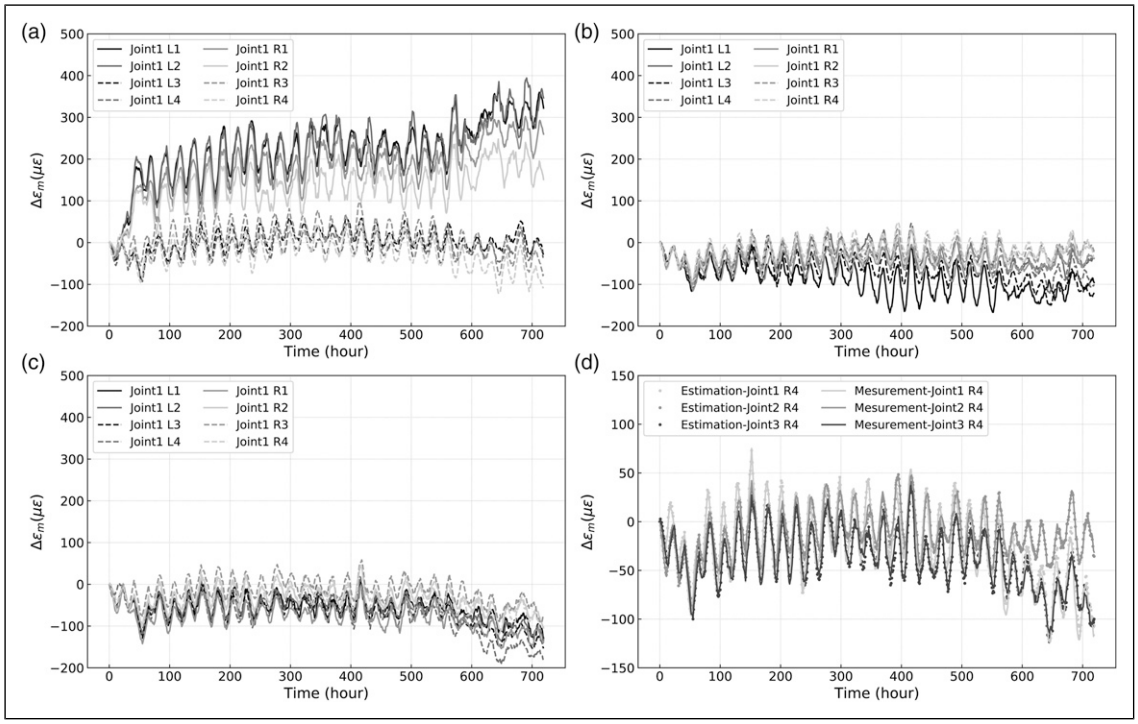

Figure 29. Estimation of ε_m within the eight nearest spatial resolution windows around (a) Joint 1, (b) Joint 2, (c) Joint 3, and (d) estimation values versus measurements of ε_m at R4 of Joint 1, Joint 2, and Joint 3 along Cable 3.

(see Figure 25). Since the top surface area of the BCOA is much larger than that of the cross section, thermal conduction through the two ends can be neglected. Thus, the temperature was assumed to be constant along each fiber and equal to the corresponding thermal couple measurement.

The experimental observation shows that it took a long time for a crack to initiate at the joint. However, after the crack opened, it propagated to the concrete bottom within a short time. When crack initiation was observed, readings were taken every hour continuously for 30 days to monitor the crack propagation through the concrete–asphalt interface. The BSS readings were recorded by Omnisens DITEST under the BOTDR mode.

Results and discussion

Unlike the wood board test, temperature compensation of the strain cable data using equation (2) was necessary due to the significant daily temperature variation. Estimation of ε_m was conducted from the BSS data measured by the Omnisens system using the developed BSS-based crack analysis method following the same procedure as the section Wood Board Separation Laboratory Test. By taking the first readings as the baseline, the increment of the estimated ε_m, ε_m, in the nearest eight SRWs around each of the three joints along Cable 1 is plotted in Figure 27. The SRWs are labeled by the position of their center points. For example, the center points of the nearest eight SRWs around Joint 1 along Cable 1 are as shown as the black points in Figure 25(b). The SRWs with the center on the left and the right of Joint 1 are labeled by "L" and "R," respectively. The following number indicates the order of the distance from the joint. "1" corresponds to the nearest SRW while "4" corresponds to the furthest one; that is, L1 is nearest to Joint 1, whereas L4 is furthest to Joint 1 in Figure 25(b). The other SRWs around the other joints along the other cables are labeled in the same way.

All the curves in Figure 27 show the daily fluctuation due to thermal expansion and contraction of the BCOA itself. Except for the four curves of Joint 1, Joint 1 L1 and 2 and Joint R1 and 2 in Figure 27(a), the other curves show an overall descending trend due to the seasonal decrease in temperature during autumn. ε_m of the eight curves near Joint 1 are the same during the first twenty-eight hours. After that, the curves dispersed from each other, indicating crack opening through the concrete–asphalt interface. At L1, L2, and R1, ε_m increased with time to 921 $\mu\varepsilon$, suggesting that the crack was generating at the overlapping area of the SRWs of L1, L2, and R1. ε_m of R2 is smaller than that of L1, L2, and R2; that is, the left boundary of SRW-R2 is within the partially debonding zone around the crack. The close examination of the data after crack development (the left side of the dashed line in Figure 27(a)) shows that the peaks of ε_m of L1, L2, and R1 correspond to the troughs of the other points along Cable 1. The crack closes and opens by the daily thermal expansion and contraction of the slab, respectively.

Different from Joint 1, the ε_m values at the points around Joint 2 and Joint 3 do not disperse from each other, as shown in Figure 27(b) and (c). The surface cracks at these joints did not penetrate to the asphalt layer. An overall decrease of about 130 $\mu\varepsilon$ and the daily fluctuation of about 50 $\mu\varepsilon$ are observed among all plots in Figure 27(b) and (c). The slight difference among them came from the structure heterogeneity. The ε_m values derived from the BSS measurements as well as the strain measurements from the Omnisens system at R4 of the three joints are shown in Figure 27(d). Since the influence of crack development on the strain measurement is negligible at this location, the data all match well to each other. Similar observations can be made from the data of Cables 2 and 3, as shown in Figures 28 and 29, respectively. The crack strains measured at Joint 1 of Cables 2 and 3 are smaller than those measured at Joint 1 of Cable 1.

The strain profiles estimated from ε_m within the SRWs along the three cables are shown in Figure 30. The peak

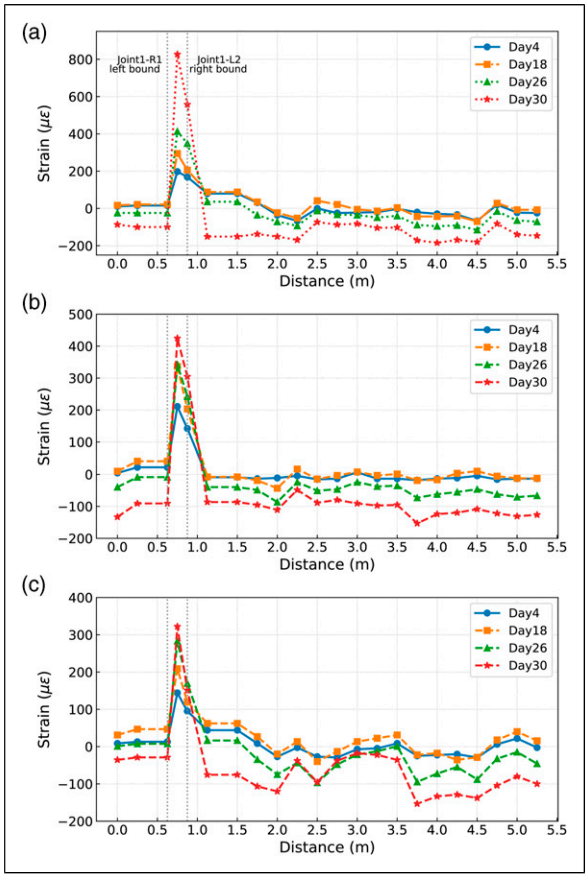

Figure 30. Estimated strain profiles along (a) Cable 1 (b) Cable 2 (c) Cable 3.

Table 2. Summarization of estimated and measured crack widths.

Cable no.	Day4	Day18	Day26	Day30	Measurement on day30
Cable1-Joint1	0.035 mm	0.052 mm	0.109 mm	0.252 mm	0.28 mm
Cable2-Joint1	0.054 mm	0.079 mm	0.099 mm	0.138 mm	—
Cable3-Joint1	0.024 mm	0.030 mm	0.063 mm	0.089 mm	0.06 mm

strain occurs between the left bound of the SRW at R1 ($x = 0.625$ m) and the right bound of the SRW of L2 ($x = 0.875$ m) and the two bounds are shown by the two vertical dashed lines. The ε_m values of L1, L2, and R1 are equal to the crack strain ε_c. By assuming the center locations of Slab1 and Slab2 are fixed, the crack sizes can be estimated by taking the sum of the fiber elongation of the left and the right part of the crack. The estimated crack sizes on Day 4, 18, 26, and 30 for the three cables are listed in Table 2. Results show that, on Day 30, the crack size at Cable 1 is 0.252 mm, whereas that at Cable 3 is 0.089 mm. The crack size at the bottom of the concrete slab from the side edge locations was measured by a vernier caliper with a measurement precision of 0.02 mm. The measurement at the edge near Cable1 was 0.28 mm, whereas that at the edge near Cable 3 was 0.06 mm. As the manual measurement was conducted at the edge of the concrete layer rather than inside the asphalt layer, the measured values are slightly different from the estimated one.

Conclusions

This study proposed a BSS-based crack analysis method to overcome the limitation of localized strain measurement caused by the low spatial resolution issue of BOTDA/R system. The method was validated through a wood board separation laboratory test. Its accuracy of (i) identifying the crack position, (ii) estimating the crack strain, and (iii) measuring the crack size was examined. The method was applied in the field to monitor the transverse joint propagation through the asphalt–concrete interface of a thin BCOA pavement.

The number of local minimums of the BSS gradient depends on both (i) the stressed area compared to the spatial resolution (r_c) and (ii) the peak strain of crack (ε_c). When BSS has double minimums, the local minimum with the largest frequency coordinate is proved to estimate the tensile strain induced by the crack. When BSS has a single minimum, crack is detectable when the crack strain dominates the BSS gradient minimum. Results from the wood board separation test show that the proposed method is able to extract the maximum strain value within the spatial resolution near the crack and to evaluate the crack size accurately. It was capable of detecting a narrow crack as small as 0.23 mm using a BOTDA analyzer with a low spatial resolution of 750 mm. The method also successfully detected the crack penetration and growth through the concrete–asphalt interface of a thin BCOA pavement.

This article describes the method of extracting the maximum strain within the SRW from the BSS measurements. For future work, the method of decomposing the BSSs into the strain profile within the SRW can be investigated. Moreover, various shapes of crack strain profile under different mechanisms, such as torsion, shear, and bending, can also be explored.

Acknowledgements

The construction of the thin BCOA for the field test in this study is supported by John Harvey, Angel Mateos, Rongzong Wu, Fabian Paniagua, and Julio Paniagua from the University of California Pavement Research Center. The authors thank Peter Hubbard and Hayato Nonaka from the University of California, Berkeley, for reviewing the manuscript.

Funding

The author(s) disclosed receipt of the following financial support for the research, authorship, and/or publication of this article: This material is based on work supported by the National Science Foundation under Grant CMMI-1741042 and by the Center for Information Technology Research in the Interest of Society (CITRIS).

ORCID iDs

Ruonan Ou https://orcid.org/0000-0001-7985-0988
Linqing Luo https://orcid.org/0000-0002-7073-6588

References

1. Sieńko R, Zych M, Bednarski Ł, et al. Strain and crack analysis within concrete members using distributed fibre optic sensors. *Struct Health Monit* 2019; 18: 1510–1526. DOI: 10.1177/1475921718804466.
2. Feng Q, Kong Q, Huo L, et al. Crack detection and leakage monitoring on reinforced concrete pipe. *Smart Mater Struct* 2015; 24: 115020. DOI: 10.1088/0964-1726/24/11/115020.
3. Yao Y, Tung S-TE and Glisic B. Crack detection and characterization techniques—an overview. *Struct Control Health Monit* 2014; 21: 1387–1413. DOI: 10.1002/stc.1655.
4. Xiao Z, Yamada K, Inoue J, et al. Fatigue cracks in longitudinal ribs of steel orthotropic deck. *Int J Fatigue* 2006; 28: 409–416. DOI: 10.1016/j.ijfatigue.2005.07.017.

5. Ohtsu M. *Acoustic emission and related non-destructive evaluation techniques in the fracture mechanics of concrete: fundamentals and applications*. Cambridge, UK: Woodhead Publishing, 2015.
6. Abu Dabous S, Yaghi S, Alkass S, et al. Concrete bridge deck condition assessment using IR thermography and ground penetrating radar technologies. *Autom Constr* 2017; 81: 340–354. DOI: 10.1016/j.autcon.2017.04.006.
7. Sun H, Pashoutani S and Zhu J. Nondestructive evaluation of concrete bridge decks with automated acoustic scanning system and ground penetrating radar. *Sensors* 2018; 18: 1955.
8. Deng F, Huang Y, Azarmi F, et al. Pitted corrosion detection of thermal sprayed metallic coatings using fiber Bragg grating sensors. *Coatings* 2017; 7: 35.
9. Smith GM, Higgins O and Sampath S. In-situ observation of strain and cracking in coated laminates by digital image correlation. *Surf Coat Technol* 2017; 328: 211–218.
10. Xu Y, Bao Y, Chen J, et al. Surface fatigue crack identification in steel box girder of bridges by a deep fusion convolutional neural network based on consumer-grade camera images. *Struct Health Monit* 2019; 18: 653–674.
11. Kechavarzi C, Soga K, De Battista N, et al. *Distributed fibre optic strain sensing for monitoring civil infrastructure*. London, UK: Ice Publishing, 2016.
12. Wang X, Shi B, Wei G, et al. Monitoring the behavior of segment joints in a shield tunnel using distributed fiber optic sensors. *Struct Control Health Monit* 2018; 25: e2056. DOI: 10.1002/stc.2056.
13. Bao Y, Valipour M, Meng W, et al. Distributed fiber optic sensor-enhanced detection and prediction of shrinkage-induced delamination of ultra-high-performance concrete overlay. *Smart Mater Struct* 2017; 26: 1–12. DOI: 10.1088/1361-665X/aa71f4.
14. Rui Y, Kechavarzi C, O'Leary F, et al. Integrity testing of pile cover using distributed fibre optic Sensing. *Sensors (Basel)* 2017; 17: 2949. DOI: 10.3390/s17122949.
15. Zhang H and Wu Z. Performance evaluation of BOTDR-based distributed fiber optic sensors for crack monitoring. *Struct Health Monit* 2008; 7: 143–156.
16. Glisic B and Inaudi D. Development of method for in-service crack detection based on distributed fiber optic sensors. *Struct Health Monit* 2012; 11: 161–171. DOI: 10.1177/1475921711414233.
17. Ravet F, Bao X and Chen L. Simple approach to determining the minimum measurable stress length and stress measurement accuracy in distributed Brillouin sensing. *Appl Opt* 2005; 44: 5304–5310.
18. Yu Y, Luo L, Li B, et al. Double peak-induced distance error in short-time-Fourier-transform-Brillouin optical time domain reflectometers event detection and the recovery method. *Appl Opt* 2015; 54: E196–E202. DOI: 10.1364/AO.54.00E196.
19. Deif A, Martín-Pérez B, Cousin B, et al. Detection of cracks in a reinforced concrete beam using distributed Brillouin fibre sensors. *Smart Mater Struct* 2010; 19. DOI: 10.1088/0964-1726/19/5/055014.
20. Horiguchi T, Shimizu K, Kurashima T, et al. Development of a distributed sensing technique using Brillouin scattering. *J Light Technol* 1995; 13: 1296–1302.
21. Zou L, Ferrier GA, Afshar S, et al. Distributed Brillouin scattering sensor for discrimination of wall-thinning defects in steel pipe under internal pressure. *Appl Opt* 2004; 43: 1583–1588.
22. Bao X and Chen L. Recent progress in Brillouin scattering based fiber sensors. *Sensors (Basel)* 2011; 11: 4152–4187. DOI: 10.3390/s110404152.
23. Kurashima T, Horiguchi T and Tateda M. Thermal effects on the Brillouin frequency shift in jacketed optical silica fibers. *Appl Opt* 1990; 29: 2219–2222.
24. Horiguchi T, Kurashima T and Tateda M. Tensile strain dependence of Brillouin frequency shift in silica optical fibers. *IEEE Phot Technol Lett* 1989; 1: 107–108.
25. Nikles M, Thevenaz L and Robert PA. Brillouin gain spectrum characterization in single-mode optical fibers. *J Light Technol* 1997; 15: 1842–1851.
26. Naruse H, Tateda M, Ohno H, et al. Dependence of the Brillouin gain spectrum on linear strain distribution for optical time-domain reflectometer-type strain sensors. *Appl Opt* 2002; 41: 7212–7217.
27. Naruse H, Tateda M, Ohno H, et al. Deformation of the Brillouin gain spectrum caused by parabolic strain distribution and resulting measurement error in BOTDR strain measurement system. *IEICE Trans Electron* 2003; 86: 2111–2121.
28. Murayama H, Kageyama K, Naruse H, et al. Distributed strain sensing from damaged composite materials based on shape variation of the Brillouin spectrum. *J Intell Mater Syst Struct* 2004; 15: 17–25. DOI: 10.1177/1045389x04039263.
29. Naruse H and Tateda M. Trade-off between the spatial and the frequency resolutions in measuring the power spectrum of the Brillouin backscattered light in an optical fiber. *Appl Optics* 1999; 38: 6516–6521.
30. Yu Y, Luo L, Li B, et al. Frequency resolution quantification of Brillouin-istributed optical fiber sensors. *IEEE Photon Technol Lett* 2016; 28: 2367–2370. DOI: 10.1109/lpt.2016.2594084.
31. Mateos A, Harvey J, Paniagua F, et al. Accelerated testing of full-scale thin bonded concrete overlay of Asphalt. *Transp Res Rec* 2019; 2673: 404–414. DOI: 10.1177/0361198119825645.
32. Harrington DS and Fick G. *Guide to concrete overlays: sustainable solutions for resurfacing and rehabilitation existing pavements*. 3rd ed. Ames, IA: National Concrete Pavement Technology Center, Iowa State University, 2014.
33. DeSantis JW, Vandenbossche JM, Alland K, et al. Development of artificial neural networks for predicting the response of bonded concrete overlays of Asphalt for use in a faulting prediction model. *Transp Res Rec* 2018; 2672: 360–370. DOI: 10.1177/0361198118758637.

Appendix 1

Proof of equivalency of quantifying r_c from ε_{cm} profile to ε_m profile

As shown in Figure 11, the ε_{cm} profile and ε_m profile are similar in shape. Both have a flat crest in the middle and the length is L. ε_{cm} within this crest can be corrected to ε_c, the value of ε_m within this crest, according to Figures 8 and 9. ε_{cm} within the lower part of the transition zone under the crack detection limit is equal to $\varepsilon_d + \sqrt{3}\Delta v/3C_\varepsilon$ because the crack detection is not possible in this zone. However, the upper part of the transition zone of the ε_{cm} profile and the ε_m profile match to each other. Therefore, a proof that the ε_m profile can be estimated from the ε_{cm} profile as shown in Figure 11 is equivalent to showing that r_c quantified by extending the slope zones of the ε_{cm} profile (red dashed lines) till $\varepsilon = \varepsilon_d$ is close to its truth value quantified from the actual ε_m profile.

To achieve this, a series of simulations were conducted to generate the ε_{cm} profile under different sets of $\varepsilon_c - \varepsilon_d$ and r_c by calculating the BSS gradients of all the SRWs and locating the local minimums of them. The simulations are done within the crack detection possible regions (orange dotted and green back slashed areas in Figure 6). Then, r_c is estimated by extending the slope zones of the simulated ε_{cm} profiles till $\varepsilon = \varepsilon_d$ as proposed in Figure 11. The estimated r_c are compared with the actual r_c in Figure 31. The blue shade marks the area with a 10% estimation error. All the estimated points in the figure are very close to the truth value. Therefore, r_c can be quantified accurately from the ε_{cm} profile.

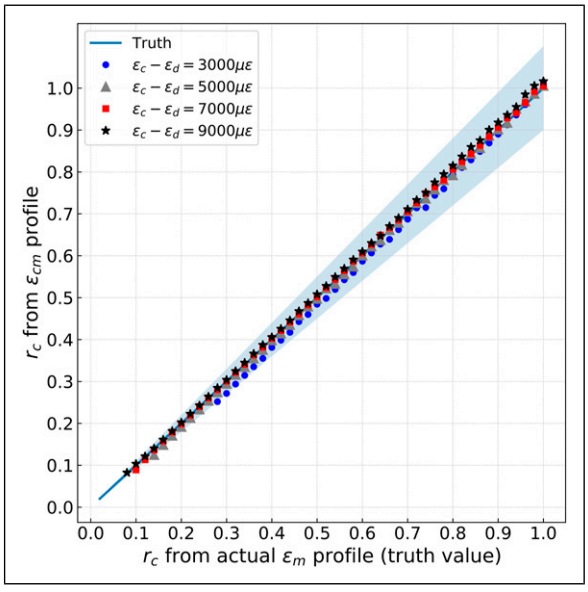

Figure 31. Truth value of r_c from ε_m profile versus estimation of r_c from ε_{cm} profile.